JCTC Journal of Chemical Theory and Computation

pubs.acs.org/JCTC Article

Coarse-Grained Molecular Simulation of Bolapolyphiles with a Multident Lateral Chain: Formation and Structural Analysis of Cubic Network Phases

Yangyang Sun and Fernando A. Escobedo*

Cite This: https://doi.org/10.1021/acs.jctc.3c00395 Read Online

ACCESS | Metrics & More | Article Recommendations | Supporting Information

ABSTRACT: Bolapolyphiles constitute a versatile class of materials with a demonstrated potential to form a wide variety of complex ordered mesophases. In particular, cubic network phases (like the gyroid, primitive, and diamond phases) have been a target of many studies for their ability to create percolating 3D nanosized channels. In this study, molecular simulations are used to explore the phase behavior of bolapolyphiles containing a rigid rodlike core, associating hydrophilic core ends and a hydrophobic side chain with a multident architecture, i.e., where the branching pattern can vary from bident (two branches) to hexadent (six branches). Upon network phase formation, its skeleton is made up of "nodes" populated by the core ends and "struts" populated by the cores. It is shown that, by varying the side chain length, branching pattern, and attachment point to the core, one can alter the crowding around the cores and hence tune the nodal size and nodal valence (i.e., number of connecting struts) which lead to different types of network morphologies. For example, for a fixed total side chain length, having more branches generates a stronger crowding around the molecular core, driving them to form bundlelike domains with curvier interfaces that result in thinner struts. Also, attaching the lateral chain closer to one core end breaks the symmetry between the environments around the two core ends, leading to networks with bimodal nodal sizes. Importantly, since the characterization of (ordered or partially ordered) network phases is challenging given the potential incompatibilities between the simulation box size with the structure's space group periodic symmetry and the effect of morphological defects, a detailed framework is presented to analyze and fully characterize the unit cell parameters and structure factor of such systems.

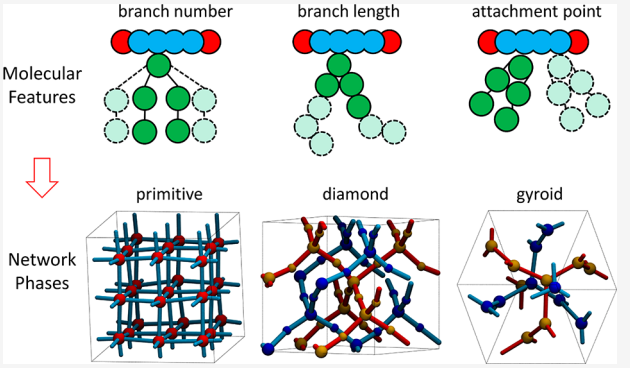

1. INTRODUCTION

Liquid crystals (LCs) have attracted significant attention for both fundamental scientific research and commercial engineering applications due to their unique combination of structural order and individual molecular fluidity.[1] Among LCs, thermotropic bolapolyphiles stand out for their molecular design versatility which can be associated with a large library of potential building blocks and the resulting complexity and richness of their mesophase behavior.[2] A typical bolapolyphilic molecule contains at least three mutually incompatible segments (e.g., see Figure S1), in which a rodlike rigid π-conjugated core is often used as the molecular backbone decorated with hydrophilic glycerol groups at both ends and with flexible lipophilic chains attached laterally. The rodlike rigid core can provide the necessary shape anisotropy to promote intermolecular alignment, and the self-attractive glycerol group can generate the driving force for nanoscale segregation by forming hydrogen bonds.[1] Adding a flexible lateral chain as the third incompatible segment can largely expand the mesophase morphology from simple smectic phases with one-dimensional (1D) periodicity[3] to columnar phases with two-dimensional (2D) periodicity[4] to complex cubic phases with three-dimensional (3D) periodicity.[5,6]

Extensive experimental efforts have been made to design new bolapolyphiles and study their self-assembling behavior. To alter the shape anisotropy, different lengths for the π-conjugated rods have been investigated by connecting different number of benzene rings, thiophene rings, and ethynylene groups;[7−10] glycerol groups are often used as the terminal groups for the rigid rod. To get tunable intramolecular amphiphilicity, a variety of lateral chain chemistries have been examined including alkyl and semiperfluoroalkyl chains[4,7] and oligo(dimethylsiloxane) and carbosilane chains.[11,12] To modify the interfacial curvature between the immiscible nanosegregated domains, linear[4,7] and branched[5,6] lateral chains

Special Issue: Computational and Theoretical Studies Focused on Self-Assembly and Molecular Organization

Received: April 6, 2023

have been studied and several attaching arrangements explored, leading to bolapolyphiles of T-shape,[7] X-shape,[13] and π-shape.[14] For each choice of bolapolyphile shape and chemistry, the relative lengths of the incompatible segments were also varied and found to play an important role in shaping the self-assembled structures.[4]

The functionality of an LC material depends strongly on the structural features and molecular packing details of its ordered mesophase. Bicontinuous cubic phases, with their unique 3D continuous structures and large internal interfacial areas, have received significant interest for their promising applications as templates and structure-directing agents to fabricate mesoporous materials,[15,16] nanofiltration membranes,[17] energy storage and conversion devices,[18−21] photonic crystals,[22−24] and biophotonic structures.[25,26] Bicontinuous phases can be constructed either by two identical or enantiomorphic networks separated by a triply periodic minimal surface[27] or by a single network embedded in a continuous domain (albeit the latter cases are sometimes referred to as cocontinuous phases). Depending on the symmetry, three types of networks are often observed, and six distinct phases can be constructed based on the number of interpenetrating networks, namely, the single and double gyroid (SG and DG), the single and double diamond (SD and DD), and the single and double plumber's nightmare or primitive (SP and DP) cubic phases. Recent studies of bolapolyphiles have already demonstrated their ability to generate the SP,[28] SD,[29] DD[6] and DG[14,30−32] phases.

By virtue of their complex and diverse chemical structures, bolapolyphiles are able to form many intricate mesoscale structures. However, these systems also pose significant challenges to predictive modeling approaches which could help unveil some of the relations between molecular design and phase behavior. In principle, molecular dynamics (MD) simulations can provide complementary information to understand and predict the molecular self-assembly behavior. However, simulations employing detailed atomistic force fields cannot be run for the times needed to observe the spontaneous self-assembly process of complex mesophases given the computational budgets typically available. This limitation can be circumvented by coarse-grained models, which simplify the molecular descriptions to make simulation much more efficient while still capturing the key physical interactions that drive the self-assembly behavior.[33−40] In this work, we apply a coarse-grained (CG) model developed in our previous study[33,34] to further explore how variations in the design of bolapolyphiles affect their mesophase behavior. Our CG model is generic as it does not provide a direct mapping between each CG bead and a specific chemistry, and it is therefore expected to primarily provide qualitative insights into the trends of mesophase formation without reproducing the exact phase behavior of specific systems. In particular, we studied bolapolyphilic molecules having different types of branched lateral chains and different points of attachment. Our simulations demonstrate that most of the bicontinuous cubic phases known experimentally can be formed by suitable designs of the lateral branched chain.

Also importantly, the structural analysis of 3D bicontinuous ordered network phases can be challenging, as the shape, relative dimensions, and orientation of the underlying crystal unit cell are system dependent. The challenges are compounded when dealing with simulated systems where box sizes are typically small, fitting only a few unit cells, thus creating significant finite size effects. While simulating systems of different sizes were required to account for such effects, structural defects are unavoidable and can render the structure factor derived from the simulated configurations difficult to interpret as it may exhibit diffraction peaks at positions which are inconsistent with those of standard model networks. To address this issue, in this work we also detail a methodological framework to analyze the simulated structure factors to fully characterize the morphological geometry of the various network phases generated by the bolapolyphiles studied.

The rest of the paper is organized as follows. In section 2 we present the molecular model of the systems to be investigated, and in section 3 we describe the simulation and analysis methods. In section 4 we present our main results, and in section 5 we summarize our main findings and provide an outlook of possible extensions.

2. MODEL

All interactions and properties in our simulation are reported in terms of the usual reduced units. The fundamental quantities required to calculate the reduced form are m_0 as the characteristic mass, σ as the characteristic distance, and ϵ as the characteristic energy. The reduced quantities are written with an asterisk:

$$m^* = \frac{m}{m_0}, \quad x^* = \frac{x}{\sigma}, \quad E^* = \frac{E}{\epsilon}$$

.

2.1. Coarse-Grained Model and Force Field Parameters.

In our CG model, the π-conjugated core and the terminal glycerol groups are constructed by a linear rigid core of CG beads with a bonded distance of 0.7σ. The flexible lateral chain attached to the core is described by a bead−spring model. Three types of CG beads are defined to discriminate different interaction strengths between incompatible segments in the bolapolyphiles (Figure 1a). Type GY (mnemonic for glycerol) beads are located at the two ends of the rigid core to act as strong self-attractive sites, akin to the glycerol group. Type PH (mnemonic for phenyl) beads constitute the central section of the rigid core to represent the typical polyphenyl core having a relatively weak PH−PH interaction. Type AK (mnemonic for

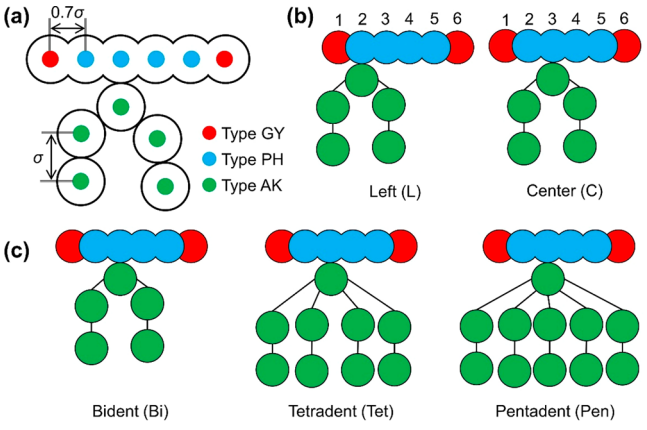

Figure 1. Topology of CG model for bolapolyphilic molecules. (a) Reference labels for CG bead types in the force field. (b) Attaching arrangements of the lateral chain to the rigid backbone or "core". (c) Representative lateral chain shapes. Bead colors are GY = red, PH = blue, and AK = green.

https://doi.org/10.1021/acs.jctc.3c00395
J. Chem. Theory Comput. XXXX, XXX, XXX−XXX

alkyl) beads form the lateral chain to mimic alkyl and semiperfluoroalkyl chains with a moderate AK−AK interaction.

The cut-and-shifted Lennard-Jones (LJ) potential is used to describe all the nonbonded interactions, including all intermolecular and intramolecular interactions between beads separated by two or more bonds:

$$U_{\mathrm{CSLJ}} = \begin{cases} U_{\mathrm{LJ}}(r_{ij}) - U_{\mathrm{LJ}}(r_{\mathrm{cut},ij}), & r_{ij} \le r_{\mathrm{cut},ij} \\ 0, & r_{ij} > r_{\mathrm{cut},ij} \end{cases} \quad (1)$$

$$U_{\mathrm{LJ}}(\zeta_{ij}) = 4\epsilon_{ij}\left[\left(\frac{\sigma_{ij}}{\zeta_{ij}}\right)^{12} - \left(\frac{\sigma_{ij}}{\zeta_{ij}}\right)^{6}\right] \quad (2)$$

where r_{ij} is the distance between CG sites i and j; σ_{ij}, ϵ_{ij}, and $r_{\mathrm{cut},ij}$ are the van der Waals diameter, the well-depth parameter, and the cutoff distance, respectively, which are all defined by the corresponding CG site types. The LJ potentials between beads separated by one bond and between any two beads within the same rigid core are turned off. The LJ potential parameters are listed in Table 1; all beads are neutral with the same mass ($m^* = 1$) and the same van der Waals diameter. Most nonbonded interactions have $r_{\mathrm{cut}} = 2^{1/6}\sigma$, leading to the purely repulsive potential known as the Weeks−Chandler−Andersen (WCA) potential.[41] Only like interactions of GY and AK beads have an attractive well with different depths to reflect the interaction strength. Compared with the original model,[33] a larger value of 0.9ϵ is chosen for AK beads to enhance phase segregation. Note that our choice of interbead interactions creates a sufficient driving force for the three types of beads (GY, AK, and PH) to microsegregate from each other. In this context, the WCA-type PH−PH interactions can be seen as being effectively "attractive" because these beads are immersed in a "poor solvent" medium and indeed tend to bundle together; however, given its CG nature, our model is unable to capture specific packing details such as the $\pi-\pi$ stacking of planar ring structures.

Table 1. Nonbonded Potential Parameters for Bolapolyphilic Molecule

CG bead type i	CG bead type j	σ_{ij}/σ	ϵ_{ij}/ϵ	$r_{\mathrm{cut},ij}/\sigma$
GY	GY	1.0	1.0	2.0
PH	PH	1.0	1.0	$2^{1/6}$
AK	AK	1.0	0.9	2.0
GY	PH	1.0	1.0	$2^{1/6}$
GY	AK	1.0	1.0	$2^{1/6}$
PH	AK	1.0	1.0	$2^{1/6}$

A harmonic bonding potential is used to for the bonded interaction between two beads in the lateral chain separated by a single bond and between the two beads connecting the rigid core and the lateral chain (i.e., PH−AK and AK−AK pairs):

$$U_{\mathrm{bond}} = K_{\mathrm{b}}(r - r_0)^2 \quad (3)$$

where K_{b} is the bond spring constant ($=25\epsilon\sigma^{-2}$), r_0 is the equilibrium bond distance ($=1.0\sigma$), and r is the separation distance between two bonded beads.

2.2. Molecular Structure. In this study, the number of beads in the rigid core (N_{rigid}) is fixed at six with two GY beads at the ends and four PH beads in the middle. Based on the chemistry, four beads in the middle of the core are available to attach a lateral chain, but due to symmetry there are only two distinct ways to do so. The CG beads in the core are numbered from one end to the other, with the terminal bead closer to the attached chain set as bead1. Then, the two types of attaching arrangement are defined as the "left" arrangement if the lateral chain attaches to bead2 and the "center" arrangement if the chain attaches to bead3 (Figure 1b).

Our previous studies investigated the phase behavior of linear (one branch) and swallowtail or bident (two branches) lateral chains. Following those inroads, here we further simulate a "multident" lateral chain having more branches. The basic information on each chain shape is summarized in Table 2, and some of them are shown in Figure 1c. In searching different complex mesophases, the number of beads in the flexible lateral chain (N_{flx}) was varied within a range. Due to the nature of each chain shape, each branch may not have the same length for a specific value of N_{flx}. However, we distribute the beads in each branch as evenly as possible; i.e., the difference between the longest and shortest branch is set as one at most.

Table 2. Lateral Chain Shape of Bolapolyphilic Molecules Explored in the Simulation[a]

shape	abbrev	N_{branch}	N_{flx}(min)
bident	Bi	2	3
trident	Tri	3	4
tetradent	Tet	4	5
pentadent	Pen	5	6
hexadent	Hex	6	7

[a] N_{flx}(min) is the minimum number of beads in the lateral chain required to form the corresponding shape.

3. SIMULATION METHODS

3.1. Molecular Dynamics Protocols. Molecular dynamics (MD) simulations were performed using LAMMPS,[42,43] and the results were visualized using VMD.[44] The molecular packing fraction is found from

$$\eta = \frac{V_{\mathrm{mol}}N}{V_{\mathrm{box}}} \quad (4)$$

where V_{box} is the volume of the simulation box, V_{mol} is the molecular volume, and N is the number of molecules in the system. V_{mol} is estimated by assuming the rigid core has spherocylindrical geometry and the beads in the lateral chain have spherical geometry (with the bead diameter equal to the van der Waals diameter); thus

$$V_{\mathrm{mol}} = V_{\mathrm{rigid}} + V_{\mathrm{flx}} = \left(3.5\frac{\pi\sigma^3}{4} + \frac{\pi\sigma^3}{6}\right) + \left(N_{\mathrm{flx}}\frac{\pi\sigma^3}{6}\right) \quad (5)$$

where V_{flx} is the volume of the flexible lateral chain with N_{flx} beads and V_{rigid} is the volume of the rigid core with its six beads (whose partial overlap is accounted for by suitable prefactors[34]).

All our simulations were performed in the canonical ensemble (NVT) with a fixed effective packing fraction $\eta = 0.45$, which is consistent with a typical dense fluid phase.[45] Periodic boundary conditions were applied in the simulation box, and the velocity-Verlet algorithm with an integration step size of $\Delta t^* = 0.005$ was used to integrate the equations of motion. The reduced time is calculated by the characteristic

https://doi.org/10.1021/acs.jctc.3c00395
J. Chem. Theory Comput. XXXX, XXX, XXX−XXX

time, $t^* = t/\sqrt{m\sigma^2/\epsilon}$. The Nosé−Hoover thermostat with a damping parameter of $\Delta\tau = 0.5$ was used to maintain the temperature constant. The reduced temperature and pressure are $T^* = k_BT/\epsilon$ and $p^* = p\sigma^3/\epsilon$, where k_B is Boltzmann's constant. To find the ordered mesophases, a gradual quench process was implemented where the system was initially simulated at a relatively high temperature to reach a well-equilibrated isotropic state. The system was then cooled in steps of $\Delta T^* = 0.2$ over a period of $t^* = 50\,000$ and equilibrated at each temperature for another $t^* = 150\,000$ period, whose final configuration was used as input for the next quench step. After several quench steps, the system reached the lowest preset temperature. Based on our observations, most of the systems exhibited the isotropic state for $T^* \geq 1.7$ and ordered phases for $T^* \leq 1.0$; therefore, the quench process was restricted to the $0.5 \leq T^* \leq 2.0$ range. This quench process was effective in exploring the mesophases associated with different molecular designs but is not indicated to find precise transition temperatures for the phases thus found.

Finite size effects play a significant role in the formation of some ordered phases, and the system size (N) or the cubic simulation box length (L_{box}) at constant density needs to be treated as an additional simulation variable. The lamella and columnar phases which typically only possess 1D and 2D periodicities, respectively, are largely insensitive to the simulation box length since their morphologies can easily rotate in space to fit inside the simulation box. On the contrary, phases with 3D periodicity are sensitive to the box length which should ideally be commensurate with a multiple integer of the corresponding unit cell length. At the same thermodynamic conditions, an inappropriate box length may frustrate the appearance of a 3D-periodic phase and lead instead to the appearance of metastable phases. Unfortunately, the unit cell dimension of a potential 3D-periodic phase is not known *a priori*. Thus, for a given molecular structure, multiple simulations with different box lengths were often performed to probe their commensurability with the unit cell length of 3D-periodic phases and to test the stability of these phases.

3.2. Network-Skeleton Analysis. Both bicontinuous cubic phases with periodic networks and disordered network phases are often observed in our simulations. The network structure can be conveniently traced by the assembly geometry of the rigid cores. As illustrated in Figure 2a, several cores bundle together to form a strut, and several struts merge into one node stabilized by the strong attraction among GY beads. Each strut can merge into two nodes at both ends, and a pair of nodes can be connected by a strut. These observations form the basis of a framework to characterize the network structures, in which a node is defined as a cluster of GY beads and a strut is defined as a bundle of cores. The key steps of this analysis are as follows:

(i) Group GY beads into network nodes. The DBSCAN algorithm (for density-based spatial clustering of applications with noise)[46] is applied to group all GY beads into different nodes. For each bead, other beads are considered neighbors if they are within a 1.5σ distance. For a bead to be considered part of a core, the minimum number of beads in its neighborhood is set to four. After clustering, the total number of nodes in the configuration (N_{node}) and the size of each node (NB_{node} = number of beads contained) are collected.

(ii) Group molecular cores into network struts. A pair of nodes are identified for each core based on the cluster information on its GY beads. Cores associated with the same pair of nodes are classified as one strut. After all cores are classified, the total number of struts in the configuration (N_{strut}) and the size of each strut (NC_{strut} = number of cores contained) are collected. The rare case where two GY beads from the same core are clustered into the same node is excluded from the analysis.

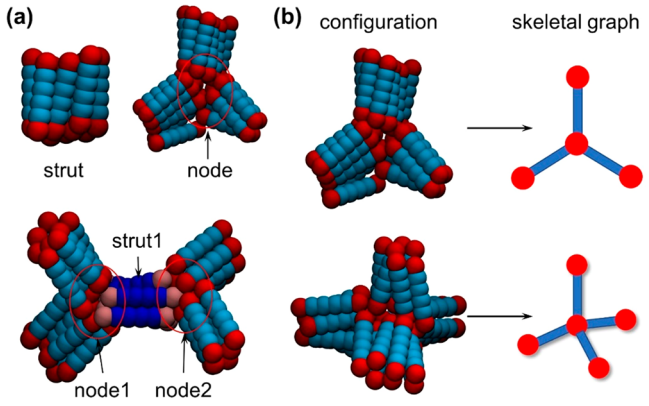

Figure 2. Schematic diagram of network-skeleton analysis. (a) Definition of the node and strut in the network structure. (b) Illustration of the skeletal graph from the corresponding simulated configuration.

(iii) Determine the interconnectivity of network nodes. Any two nodes associated with the same strut are interconnected. For a given node, the number of its interconnected nodes is the nodal valence (ν), a key feature for different network structures (e.g., the gyroid, diamond, and plumber's nightmare networks have nodal valences of $\nu = 3$, 4, and 6, respectively).

(iv) Draw the skeletal graph of the network, wherein a straight line is drawn between the centers of mass of two interconnected nodes (Figure 2b). Compared to the simulated configuration, a skeletal graph provides a simpler representation of any network structure.

Overall, the network-skeleton analysis can be applied to both ordered and disordered network structures to identify their basic building units. Several quantitative parameters can be calculated for comparison with different model network structures.

3.3. Structure Factor. The unique space group symmetries of different ordered structures can be identified by the simulated diffraction patterns. In our CG model, beads of different types are assumed to have the same scattering factor, and the structure factor, $S(\boldsymbol{q})$, is calculated using a simplified form:[47]

$$S(\boldsymbol{q}) = \frac{1}{N_{bead}}\left[\left(\sum_j \cos(\boldsymbol{q}\cdot\boldsymbol{r}_j)\right)^2 + \left(\sum_j \sin(\boldsymbol{q}\cdot\boldsymbol{r}_j)\right)^2\right] \quad (6)$$

where $\boldsymbol{q}$ is the scattering vector, $\boldsymbol{r}_j$ is the position vectors of bead j forming the structure, and N_{bead} is the number of beads forming the structure. The positions of either both GY and PH beads or only GY beads were used in this calculation, depending on the objective of the analysis (which is specified for each system). Indeed, for bicontinuous cubic phases formed in our simulations, $S(\boldsymbol{q})$ can be calculated either using GY beads only to identify the periodic symmetry of network nodes or using both GY and PH beads to confirm the overall network symmetry (nodes + struts). Since the AK beads in the

https://doi.org/10.1021/acs.jctc.3c00395
J. Chem. Theory Comput. XXXX, XXX, XXX−XXX

flexible lateral chains just pack disorderly, filling in the continuous domain surrounding the rigid cores, it is convenient to exclude them from the $S(\boldsymbol{q})$ calculation to thus obtain diffraction patterns with better defined peaks. Due to the periodic boundaries, the scattering vector is restricted to integer numbers of wavelengths within the simulation box, which in practice is generated from the reciprocal box vectors. Only a cuboid box shape is considered henceforth, so the box vectors in real space ($\boldsymbol{L}_x$, $\boldsymbol{L}_y$, $\boldsymbol{L}_z$) and in reciprocal space ($\boldsymbol{L}_x^*$, $\boldsymbol{L}_y^*$, $\boldsymbol{L}_z^*$) are given by

$$\begin{bmatrix} \boldsymbol{L}_x \\ \boldsymbol{L}_y \\ \boldsymbol{L}_z \end{bmatrix} = \begin{bmatrix} L_x & 0 & 0 \\ 0 & L_y & 0 \\ 0 & 0 & L_z \end{bmatrix} \tag{7}$$

$$\begin{bmatrix} \boldsymbol{L}_x^* \\ \boldsymbol{L}_y^* \\ \boldsymbol{L}_z^* \end{bmatrix} = 2\pi \begin{bmatrix} 1/L_x & 0 & 0 \\ 0 & 1/L_y & 0 \\ 0 & 0 & 1/L_z \end{bmatrix} \tag{8}$$

where L_x, L_y, and L_z are box lengths in the x-, y-, and z-axes, and for the special case of a cubic box, $L_x = L_y = L_z = L_{box}$. Accordingly, the scattering vector can be constructed using three integers (n_x, n_y, n_z) and the reciprocal box vectors

$$\boldsymbol{q}_{nx,ny,nz} = n_x\boldsymbol{L}_x^* + n_y\boldsymbol{L}_y^* + n_z\boldsymbol{L}_z^* = 2\pi\left(\frac{n_x}{L_x}, \frac{n_y}{L_y}, \frac{n_z}{L_z}\right) \tag{9}$$

which assumes that the obtained structure is periodic (continuous) across the periodic boundaries of the simulation box. Our analysis is hence restricted to cases where the box size was not so incompatible with the phase unit cell to frustrate the network phase from forming.

The Miller index notation provides a systematic approach to describe the periodic symmetries by constructing different sets of parallel lattice planes with equal interplanar spacing, whose normal vectors are defined by the unit cell and three specific integers written as (hkl). The unit cell of a periodic structure is usually described by a parallelepiped using three lattice vectors ($\boldsymbol{a}$, $\boldsymbol{b}$, $\boldsymbol{c}$) or six lattice parameters: the lengths of three cell edges (a, b, c) and three angles between these edges (α, β, γ). The lattice vectors and the lattice parameters can be interconverted based on a suitable convention. In practice, the reciprocal lattice vectors ($\boldsymbol{a}^*$, $\boldsymbol{b}^*$, $\boldsymbol{c}^*$) are more convenient for studying a periodic symmetry. The relationships between the direct and the reciprocal lattice vectors are given by

$$\begin{cases} \boldsymbol{a}^* = \Omega\boldsymbol{b} \times \boldsymbol{c} \\ \boldsymbol{b}^* = \Omega\boldsymbol{c} \times \boldsymbol{a} \\ \boldsymbol{c}^* = \Omega\boldsymbol{a} \times \boldsymbol{b} \end{cases} \tag{10}$$

$$\begin{cases} \boldsymbol{a} = \Omega^*\boldsymbol{b}^* \times \boldsymbol{c}^* \\ \boldsymbol{b} = \Omega^*\boldsymbol{c}^* \times \boldsymbol{a}^* \\ \boldsymbol{c} = \Omega^*\boldsymbol{a}^* \times \boldsymbol{b}^* \end{cases} \tag{11}$$

where $\Omega = 2\pi/[\boldsymbol{a}\cdot(\boldsymbol{b} \times \boldsymbol{c})]$ and $\Omega^* = 2\pi/[\boldsymbol{a}^*\cdot(\boldsymbol{b}^* \times \boldsymbol{c}^*)]$. For a given group of Miller indices (hkl), the normal vector ($\boldsymbol{G}_{hkl}$) and the interplanar spacing (d_{hkl}) of the corresponding set of lattice planes are defined using the reciprocal lattice vectors as follows:

$$\boldsymbol{G}_{hkl} = h\boldsymbol{a}^* + k\boldsymbol{b}^* + l\boldsymbol{c}^* \tag{12}$$

$$d_{hkl} = \frac{2\pi}{|\boldsymbol{G}_{hkl}|} \tag{13}$$

By convention, negative integers in (n_x, n_y, n_z) and (hkl) are written with an underline, as in $\underline{3}$ for -3. The notation $\{hkl\}$ denotes the set of all Miller indices that are equivalent to (hkl) by the symmetry of the lattice. Henceforth, the Miller indexed vector is used to refer to $\boldsymbol{G}_{hkl}$. For a perfect periodic structure (to be referred to as the "theoretical model"), its unit cell is described by the lattice vectors, and beads in the unit cell are represented by their fractional coordinates in terms of the lattice vectors. The theoretical model can determine whether a group of Miller indices gives a constructive interference with nonzero diffraction intensity by calculating the amplitude and phase of the corresponding diffraction wave:

$$F_{hkl} = \sum_j f\ \exp[2\pi i(hu_j + kv_j + lw_j)] \tag{14}$$

where the sum is over all the beads in the unit cell; u_j, v_j, and w_j are the fractional coordinates of bead j; and f is the scattering factor, which is treated as a constant in our study. The diffraction intensity is given by the squared modulus, $|F_{hkl}|^2$. The complete list of Miller indices giving nonzero diffraction intensity can be found analytically by finding a general solution for F_{hkl}. Often, an incomplete list is enough to cover the range measured by the $S(\boldsymbol{q})$ plot, which can be constructed numerically by enumerating all the Miller indices up to a certain vector magnitude of $\boldsymbol{G}_{hkl}$. Note that F_{hkl} indicates that structures with different unit cell dimensions can have the same periodic symmetry (i.e., the same set of Miller indices) as long as the constituent beads arrange in the same fractional coordinates.

For the different ordered structures observed in the simulations, their periodic symmetries can be confirmed by assigning proper Miller indices predicted by the theoretical model to the diffraction peaks in the calculated $S(\boldsymbol{q})$ plot, at which the Laue condition is satisfied:

$$\boldsymbol{q}_{nx,ny,nz} = \boldsymbol{G}_{hkl} \tag{15}$$

that requires equivalence between each component of the scattering vector and the Miller indexed vector. We develop an indexing algorithm for the calculated $S(\boldsymbol{q})$ plot by following ideas similar to those used in the analysis of experimental X-ray scattering data.[48−50] Given an ordered structure, let us assume that a distinctive set of Miller indexed vectors, $\{\boldsymbol{G}_{hkl}\}$, giving nonzero diffraction intensity, is predicted by the theoretical model, and a set of scattering vectors, $\{\boldsymbol{q}_{nx,ny,nz}\}$, showing diffraction peaks, is observed in the calculated $S(\boldsymbol{q})$ plot. Based on eqs 9 and 12, the correspondence between sets $\{\boldsymbol{G}_{hkl}\}$ and $\{\boldsymbol{q}_{nx,ny,nz}\}$ can be established by finding the relationship between the reciprocal lattice vectors ($\boldsymbol{a}^*$, $\boldsymbol{b}^*$, $\boldsymbol{c}^*$) and the reciprocal box vectors ($\boldsymbol{L}_x^*$, $\boldsymbol{L}_y^*$, $\boldsymbol{L}_z^*$). A trial-and-error algorithm was implemented to find such a relationship that leads to the best match between $\{\boldsymbol{G}_{hkl}\}$ and $\{\boldsymbol{q}_{nx,ny,nz}\}$. The key steps of this algorithm are as follows:

(i) Select three Miller indexed vectors ($\boldsymbol{G}_1$, $\boldsymbol{G}_2$, $\boldsymbol{G}_3$) as a basis from the set $\{\boldsymbol{G}_{hkl}\}$ which are linearly independent and follow the right-hand rule.

(ii) Select three scattering vectors ($\boldsymbol{q}_1$, $\boldsymbol{q}_2$, $\boldsymbol{q}_3$) as a basis from the set $\{\boldsymbol{q}_{nx,ny,nz}\}$ which are linearly independent and follow the right-hand rule.

https://doi.org/10.1021/acs.jctc.3c00395
J. Chem. Theory Comput. XXXX, XXX, XXX−XXX

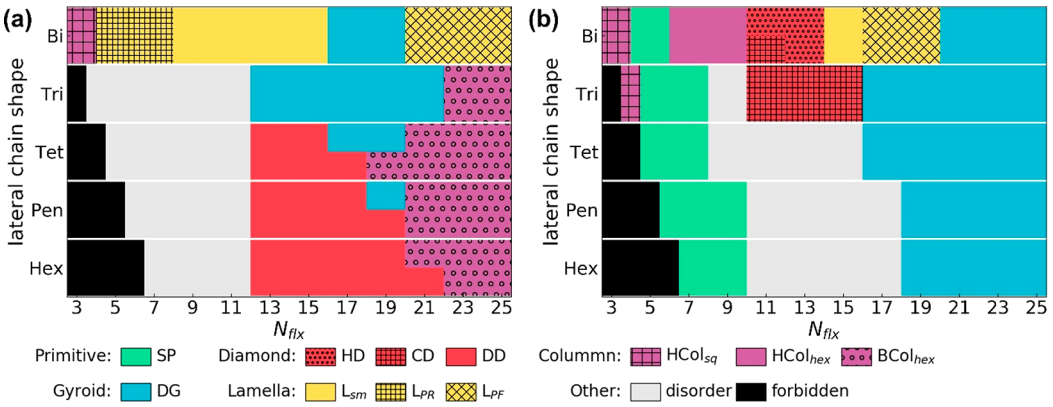

Figure 3. Simulation phase diagram of bolapolyphilic molecules studied at $T^* = 0.7$. Results for the left (a) and center (b) attaching points. Descriptions of these phases are given in the main text and Supporting Information.

(iii) Derive the relationship between $(\boldsymbol{a}^*, \boldsymbol{b}^*, \boldsymbol{c}^*)$ and $(\boldsymbol{L}_x^*, \boldsymbol{L}_y^*, \boldsymbol{L}_z^*)$ by equating the vectors:

$$\boldsymbol{G}_1 = \boldsymbol{q}_1, \quad \boldsymbol{G}_2 = \boldsymbol{q}_2, \quad \boldsymbol{G}_3 = \boldsymbol{q}_3 \tag{16}$$

(iv) Convert the set of scattering vectors, $\{\boldsymbol{q}_{nx,ny,nz}\}$, into the corresponding set of Miller indexed vectors, $\{\boldsymbol{G}_{hkl}\}_q$, using the relationship derived in step iii. Count the number of overlapping items between $\{\boldsymbol{G}_{hkl}\}$ and $\{\boldsymbol{G}_{hkl}\}_q$ as a metric to evaluate the fitting quality.

(v) Enumerate all the possible permutations of the group of three qualified vectors in $\{\boldsymbol{q}_{nx,ny,nz}\}$ by repeating steps ii–iv. Determine the best-fit relationship between $(\boldsymbol{a}^*, \boldsymbol{b}^*, \boldsymbol{c}^*)$ and $(\boldsymbol{L}_x^*, \boldsymbol{L}_y^*, \boldsymbol{L}_z^*)$, which gives the maximum overlap in step iv. Derive the direct lattice vectors $(\boldsymbol{a}, \boldsymbol{b}, \boldsymbol{c})$ in terms of the box vectors $(\boldsymbol{L}_x, \boldsymbol{L}_y, \boldsymbol{L}_z)$.

Typically, only a limited number of diffraction peaks are observed in the $S(\boldsymbol{q})$ plot due to defects in the simulated structure, and the number of items in $\{\boldsymbol{q}_{nx,ny,nz}\}$ is much fewer than in $\{\boldsymbol{G}_{hkl}\}$. For algorithmic efficiency, the choice of Miller indexed vectors, $(\boldsymbol{G}_1, \boldsymbol{G}_2, \boldsymbol{G}_3)$, is fixed in step i, and in principle, any three-vector group meeting the criteria can be selected as a basis. However, for algorithmic accuracy, the three-vector basis with the strongest diffraction intensities and smallest vector magnitudes is preferred, since these vectors are more likely to have the corresponding scattering vectors in $\{\boldsymbol{q}_{nx,ny,nz}\}$. In practice, our algorithm often finds multiple best-fit relationships between $(\boldsymbol{a}^*, \boldsymbol{b}^*, \boldsymbol{c}^*)$ and $(\boldsymbol{L}_x^*, \boldsymbol{L}_y^*, \boldsymbol{L}_z^*)$, which are equivalent in the sense of generating the same crystal lattice. Among these best-fit relationships, the corresponding lattice parameters with the highest symmetry (e.g., cubic lattice, orthorhombic lattice) will be reported in our study and the direct lattice vectors illustrated in the simulated configurations.

For the special case of cubic periodic structures, the interpretation of the $S(\boldsymbol{q})$ plots is more straightforward, not needing any trial-and-error scheme, since the magnitudes of Miller indexed vectors predicted by the theoretical model exhibit a series of simple characteristic ratios, e.g., the double gyroid phase with the ratios of ($\sqrt{6}$: $\sqrt{8}$: $\sqrt{14}$: $\sqrt{16}$: $\sqrt{20}$: $\sqrt{22}$).[51] Also, the cubic unit cell length ($a = b = c = L_{UC}$) can be roughly estimated by the position of the first diffraction peak:[52]

$$L_{UC} = \frac{2\pi}{q^*} d \tag{17}$$

where q^* is the modulus of the scattering vector at which the maximum of $S(\boldsymbol{q})$ is located and d is the first spacing ratio for a given periodic structure (e.g., $d = \sqrt{6}$ for the double gyroid phase).

4. RESULTS

4.1. Phase Diagram. Figure 3 shows a global phase diagram for bolapolyphilic molecules with differently shaped lateral chains obtained at the reduced temperature of $T^* \approx 0.7$ using the quenching approach described in section 3.1. For conciseness, each molecular structure is denoted by a combination of the lateral chain shape, the number of beads in the lateral chain (N_{flx}), and the attaching arrangement. For example, Bi13L stands for the molecular structure having a bident lateral chain with $N_{flx} = 13$ and a "left" attaching point, and Tri7C denotes a molecule having a trident lateral chain with $N_{flx} = 7$ and a "center" attaching point. In Figure 3, the black forbidden region for each chain shape is consistent with the minimum number of beads required to construct such a shape (Table 2). Several ordered mesophases are observed in the simulations, including lamella (L), honeycomb column (HCol), axial-bundled column (BCol), single primitive (SP), single hexagonal diamond (HD) network, single cubic diamond (CD) network, double diamond (DD) network, and double gyroid (DG) network. Due to the large design space covered by our simulations, it is impractical to show the simulation result explicitly for every condition explored. Instead, our discussion focuses on the main network phases of interest formed at $T^* = 0.7$ and their structural features; a brief discussion of lamellar and columnar phases is presented in the Supporting Information.

4.2. Primitive Network Phases. The primitive or plumber's nightmare network usually consists of six-way-junction nodes with octahedral geometry, which are interconnected by struts. In our simulation, the single primitive network (SP) phase was observed at some conditions (Table 3), in which the rigid cores form the network structure embedded in the continuous domain of the lateral chains (Figure 4a). Based on our network-skeleton analysis, this SP phase can be described by a basic building unit, in which the $\nu = 6$ nodes are connected by struts containing one bundle of cores (Figure 4b) and the distance between two interconnected nodes is roughly the length of the cores. In the perfect SP model, all nodes are hexavalent, and each strut is shared by

https://doi.org/10.1021/acs.jctc.3c00395
J. Chem. Theory Comput. XXXX, XXX, XXX−XXX

Table 3. Simulation Results for the SP Phase Formed at T^* = 0.7 for Specific Molecular Structures with N Molecules in a Cubic Box of Length L_{box}[a]

mol struct	N	L_{box}/σ	N_{node}	N_{strut}	ν	NB_{node}	NC_{strut}
Tri7C	400	18.34	30.9	85.9	5.57	25.9	4.57
Tet7C	400	18.34	34.3	94.7	5.53	23.4	4.13
Pen7C	400	18.34	36.9	103.4	5.61	21.7	3.75
Pen9C	400	19.22	39.7	110.9	5.58	20.1	3.53
Hex9C	400	19.22	39.8	111.0	5.58	20.1	3.52

[a]The structural features listed are the ensemble average of the number of nodes (N_{node}), struts (N_{strut}), nodal valence (ν), number of GY beads in the node (NB_{node}), and number of molecular cores in the strut (NC_{strut}).

two nodes so that the numbers of nodes and struts are related by

$$N_{strut} = 3N_{node} \tag{18}$$

However, the nodal valence distributions reflect some defects in the simulated configurations (Figure 4c), leading to a slight deviation from eq 18. A node with $\nu < 6$ indicates missing struts for pairs of interconnected nodes, while a node with $\nu > 6$ indicates the formation of extra struts that break the nodal octahedral geometry. The node size distribution shows a concentrated unimodal shape with a long tail for short sizes related to structural defects, suggesting that the nodal structure in the network is relatively uniform with no preference for the cores to aggregate within the network structure (Figure 4d). Also, the node size is concentrated at different values depending on the molecular structure, especially the lateral chain shape; a more detailed discussion is given in section 4.6.1.

Since the nodes in the SP network exhibit the simple cubic (SC) symmetry, the structure factor is calculated using the position vectors of GY beads. In theory, the unit cell of the simple cubic lattice contains one bead at (0, 0, 0) and the lattice parameters are given by

$$(a, b, c, \alpha, \beta, \gamma) = (a, a, a, 90^\circ, 90^\circ, 90^\circ) \tag{19}$$

leading to simplified forms for the Miller indexed vector ($\boldsymbol{G}_{hkl}$):

$$\boldsymbol{G}_{hkl}(\text{SC theory}) = \frac{2\pi}{a}(h, k, l) \tag{20}$$

$$G_{hkl}(\text{SC theory}) = \frac{2\pi}{a}\sqrt{h^2 + k^2 + l^2} \tag{21}$$

For the simulated SP phase formed by Tri7C, the $S(\boldsymbol{q})$ peak positions (Figure 5a) are consistent with the characteristic ratios of the simple cubic symmetry (1: $\sqrt{2}$: $\sqrt{3}$: $\sqrt{4}$: $\sqrt{5}$). The theoretical model is used to assign Miller indices to these diffraction peaks, with different indices potentially reflecting to the same peak position. Table S2 summarizes all the theoretical Miller indices up to the ratio of $\sqrt{5}$ and the corresponding diffraction peaks observed in the $S(\boldsymbol{q})$ plot of Tri7C. The unit cell length of this simulated SP phase is evaluated using eq 17 with d = 1, which turns out to be exactly one-third of the cubic simulation box length, L_{box} (Figure 5b).

Due to the relatively small unit cell length of the simulated SP phase, multiple unit cells were able to fit inside the simulation box sizes employed, with the structure able to rotate and even deform to fit into boxes over a wide range of sizes. As a result, these $S(\boldsymbol{q})$ plots often show various diffraction patterns, with their peak positions following different ratios that deviate from the theoretical model. In such cases, the trial-and-error algorithm was used to interpret the $S(\boldsymbol{q})$ plots and characterize the deformed unit cells (see Table 4). This analysis is illustrated for the Tet7C case (Figure 5c). For the simple cubic lattice, the basis of three Miller indexed vectors is chosen to be ($\boldsymbol{G}_{100}$, $\boldsymbol{G}_{010}$, $\boldsymbol{G}_{001}$). After looping through all the permutations of the basis of the scattering vectors, the following correspondence gives the optimal match between the theoretical model and the $S(\boldsymbol{q})$ plot:

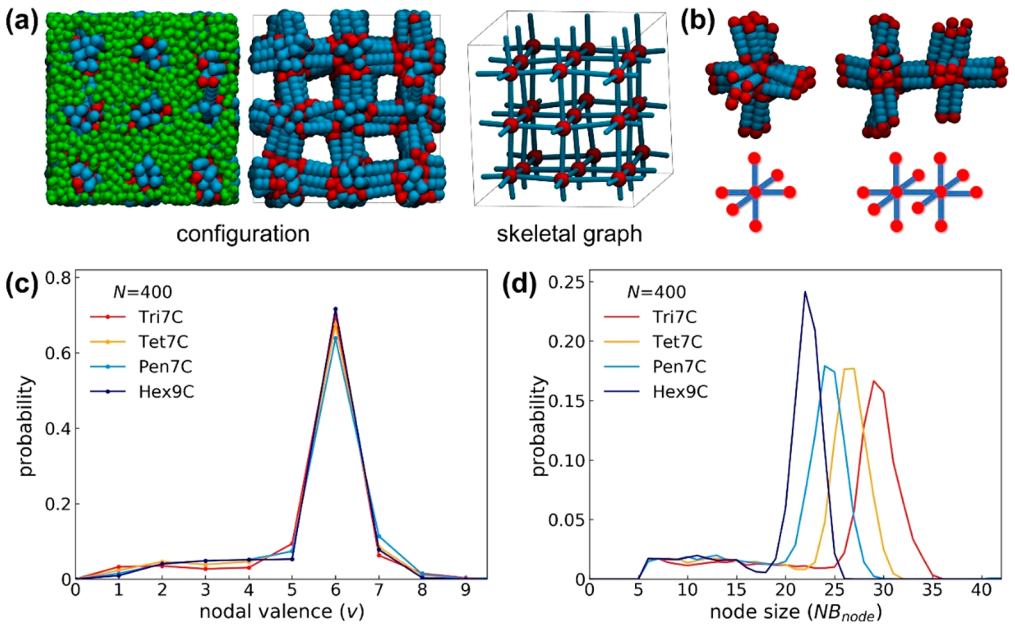

Figure 4. Network characteristics of SP phases formed at T^* = 0.7. (a) Snapshots of phase for Tri7C with N = 400. (b) Basic SP building unit. Bead colors are GY = red, PH = blue, and AK = green. For clarity, some snapshots only show the cores. Distributions of (c) nodal valence and (d) node size generated by the network-skeleton analysis of representative molecular structures.

https://doi.org/10.1021/acs.jctc.3c00395
J. Chem. Theory Comput. XXXX, XXX, XXX−XXX

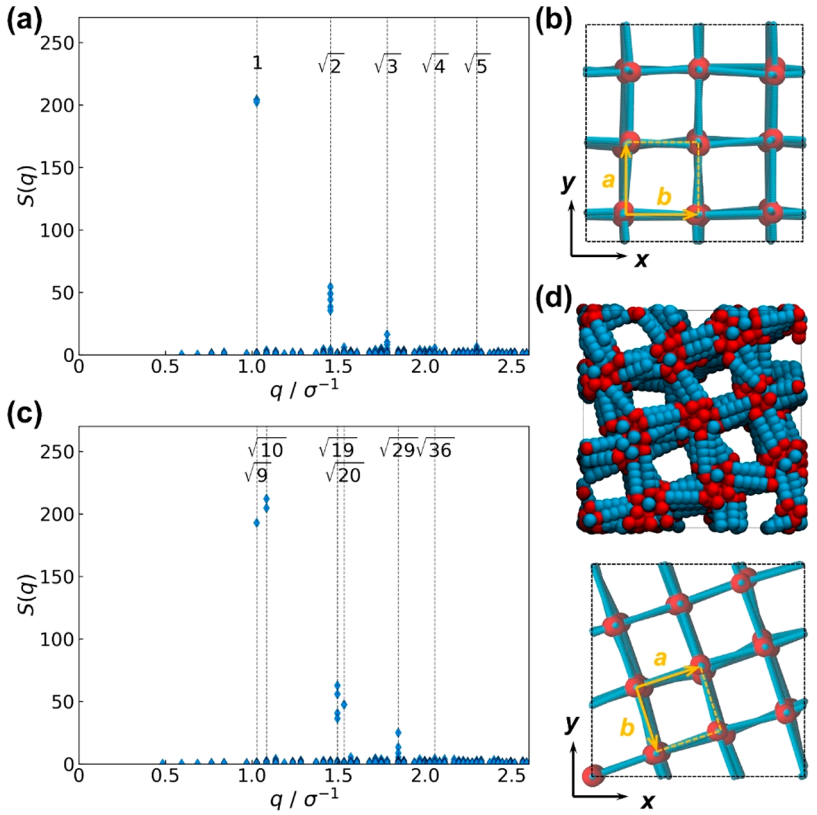

Figure 5. Structure of simulated SP phases formed at $T^* = 0.7$ and $N = 400$. (a) Structure factor and (b) skeletal graph from configuration of Tri7C. (c) Structure factor and (d) skeletal graph from configuration of Tet7C. In (b) and (d) the struts are blue, nodes are red, and the unit cell is drawn to illustrate its relationship with the cubic box vectors.

Table 4. Lattice Parameters of the SP Phase Estimated from the Structure Factor

mol struct	N	L_{box}/σ	a/σ	b/σ	c/σ	α/deg	β/deg	γ/deg
Tri7C	400	18.34	6.11	6.11	6.11	90	90	90
Tet7C	400	18.34	5.80	5.80	6.11	90	90	90
Pen7C	400	18.34	5.53	5.83	5.83	84.3	90	90
Pen9C	400	19.22	5.85	5.85	5.85	84.3	84.3	84.3
Hex9C	400	19.22	5.85	5.85	5.85	84.3	84.3	84.3

$$\boldsymbol{G}_{100} = \boldsymbol{q}_{310}, \quad \boldsymbol{G}_{010} = \boldsymbol{q}_{1\bar{3}0}, \quad \boldsymbol{G}_{001} = \boldsymbol{q}_{00\bar{3}} \tag{22}$$

Hence, the relationships between the reciprocal lattice vectors and the reciprocal box vectors are

$$\begin{cases} \boldsymbol{a}^* = 3\boldsymbol{L}_x^* + \boldsymbol{L}_y^* \\ \boldsymbol{b}^* = \boldsymbol{L}_x^* - 3\boldsymbol{L}_y^* \\ \boldsymbol{c}^* = -3\boldsymbol{L}_z^* \end{cases} \tag{23}$$

Then, proper Miller indices are assigned to the diffraction peaks in the $S(\boldsymbol{q})$ plot of Tet7C (Table S2). Given the cubic shaped box used in the simulation, the associated Miller indexed vectors and their magnitudes are calculated from ($\boldsymbol{a}^*$, $\boldsymbol{b}^*$, $\boldsymbol{c}^*$), leading to

$$\boldsymbol{G}_{hkl}(\text{SP Tet7C}) = \frac{2\pi}{L_x}(3h + k, h - 3k, -3l) \tag{24}$$

$$G_{hkl}(\text{SP Tet7C}) = \frac{2\pi}{L_x}\sqrt{10(h^2 + k^2) + 9l^2} \tag{25}$$

The direct lattice vectors are obtained from ($\boldsymbol{a}^*$, $\boldsymbol{b}^*$, $\boldsymbol{c}^*$) using eq 11, which are illustrated in the simulated configuration in Figure 5d:

$$\begin{cases} 10\boldsymbol{a} = 3\boldsymbol{L}_x + \boldsymbol{L}_y \\ 10\boldsymbol{b} = \boldsymbol{L}_x - 3\boldsymbol{L}_y \\ 3\boldsymbol{c} = -\boldsymbol{L}_z \end{cases} \tag{26}$$

Compared with the theoretical model, the $S(\boldsymbol{q})$ plots of both Tri7C and Tet7C show a limited number of diffraction peaks, which is likely related to the structural fluctuations within the finite volume occupied by the networks in the simulated configurations (contrasting the dimensionless points in the theoretical model) and some minor structural defects. While the peak positions in these two $S(\boldsymbol{q})$ plots exhibit different series of ratios, they can be designated by the same set of Miller indices, showing that these two simulated SP phases share similar periodic symmetries of the simple cubic lattice but with slightly different dimensions.

4.3. Single Diamond Network Phases. The diamond network consists of four-way-junction nodes with tetrahedral

https://doi.org/10.1021/acs.jctc.3c00395
J. Chem. Theory Comput. XXXX, XXX, XXX−XXX

Table 5. Simulation Conditions and Structural Features for the Single Hexagonal and Cubic Diamond Phases Formed at $T^* = 0.7$

phase	mol struct	N	L_{box}/σ	N_{node}	N_{strut}	ν	NB_{node}	NC_{strut}
HD	Bi11C	400	20.02	35.3	70.7	4.01	22.7	5.58
	Bi13C	400	20.77	36.0	70.7	3.93	22.2	5.57
CD	Bi11C	600	22.92	52.9	105.3	3.98	22.7	5.63
	Tri11C	400	20.02	42.1	86.0	4.09	19.0	4.52
	Tri13C	300	18.87	34.3	67.1	3.91	17.5	4.40
	Tri15C	400	21.47	43.2	84.4	3.90	18.5	4.68

geometry, which are interconnected by struts. In our simulations, two types of single diamond networks were observed at the conditions listed in Table 5: the hexagonal diamond (HD) and the cubic diamond (CD).

Based on our network-skeleton analysis, both diamond networks can be described by a similar building unit, in which the $\nu = 4$ nodes are connected by struts containing one bundle of cores, with any two interconnected nodes being roughly one core length apart. For any pair of interconnected nodes, the staggered and eclipsed conformations are identifiable (Figure 6a). In the HD phase, the ratio between the staggered and eclipsed conformations is 3:1, while in the CD phase only the staggered conformation occurs. The HD phase can be derived from the hexagonal close-packing (HCP) of equal spheres by replacing each sphere by a pair of interconnected nodes (Figure 6b). For computation simplicity and ease of visualization, a nonprimitive unit cell is adopted in our ensuing discussion. Hence, in a cuboid unit cell of the HD network, four pairs of nodes follow a two-layer stacking with a repeating AB pattern. The lattice parameters, the node positions in fractional coordinates, and strut length (L_{strut}) are

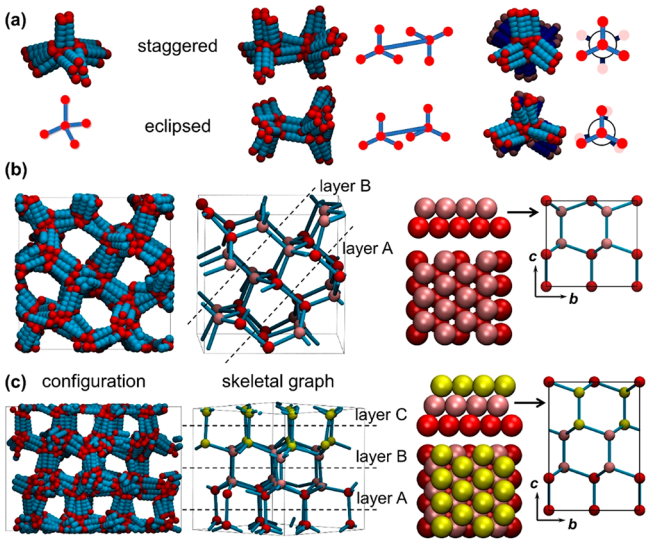

Figure 6. Simulated configurations of the HD and CD phases formed at $T^* = 0.7$. For clarity, only the cores are shown with red GY beads and blue PH beads. (a) Basic building units for the single diamond network. (b) HD phase from Bi13C with $N = 400$. In the skeletal graph, nodes are divided into different pairs, whose centers roughly align in the HCP pattern with a two-layer stacking as illustrated by the theoretical model. Struts are blue, and nodes from different layers are colored in red and pink, respectively. (c) CD phase from Bi11C with $N = 600$. In the skeletal graph, nodes are divided into different pairs, whose centers roughly align in the FCC close-packing with a three-layer stacking as illustrated by the theoretical model. Struts are blue, and nodes from different layers are colored in red, pink, and yellow, respectively.

$$(a, b, c, \alpha, \beta, \gamma) = \left(a, \sqrt{3}a, \frac{2\sqrt{6}}{3}a, 90^\circ, 90^\circ, 90^\circ\right) \tag{27}$$

$$\text{nodes}\begin{cases}\text{layer A: } (0,0,0) \quad \left(0,0,\frac{3}{8}\right); \quad \left(\frac{1}{2},\frac{1}{2},0\right) \quad \left(\frac{1}{2},\frac{1}{2},\frac{3}{8}\right)\\ \text{layer B: } \left(\frac{1}{2},\frac{1}{6},\frac{1}{2}\right) \quad \left(\frac{1}{2},\frac{1}{6},\frac{7}{8}\right); \quad \left(1,\frac{2}{3},\frac{1}{2}\right) \quad \left(1,\frac{2}{3},\frac{7}{8}\right)\end{cases} \tag{28}$$

$$L_{strut} = \left|\left(\frac{a}{2},\frac{b}{6},\frac{c}{8}\right)\right| = \left|\left(0,\frac{b}{3},\frac{c}{8}\right)\right| = \left|\left(0,0,\frac{3}{8}c\right)\right| = \frac{\sqrt{6}}{4}a \tag{29}$$

In contrast, the CD phase can be derived from the face-centered-cubic (FCC) close-packing of equal spheres by replacing each sphere by a pair of interconnected nodes (Figure 6c). Then, in a cuboid unit cell, six pairs of nodes follow a three-layer stacking with the repeating ABC pattern. The lattice parameters, node positions in fractional coordinates, and strut length are

$$(a, b, c, \alpha, \beta, \gamma) = (a, \sqrt{3}a, \sqrt{6}a, 90^\circ, 90^\circ, 90^\circ) \tag{30}$$

$$\text{nodes}\begin{cases}\text{layer A: } (0,0,0) \quad \left(0,0,\frac{1}{4}\right); \quad \left(\frac{1}{2},\frac{1}{2},0\right) \quad \left(\frac{1}{2},\frac{1}{2},\frac{1}{4}\right)\\ \text{layer B: } \left(\frac{1}{2},\frac{1}{6},\frac{1}{3}\right) \quad \left(\frac{1}{2},\frac{1}{6},\frac{7}{12}\right); \quad \left(1,\frac{2}{3},\frac{1}{3}\right) \quad \left(1,\frac{2}{3},\frac{7}{12}\right)\\ \text{layer C: } \left(0,\frac{1}{3},\frac{2}{3}\right) \quad \left(0,\frac{1}{3},\frac{11}{12}\right); \quad \left(\frac{1}{2},\frac{5}{6},\frac{2}{3}\right) \quad \left(\frac{1}{2},\frac{5}{6},\frac{11}{12}\right)\end{cases} \tag{31}$$

$$L_{strut} = \left|\left(\frac{a}{2},\frac{b}{6},\frac{c}{12}\right)\right| = \left|\left(0,\frac{b}{3},\frac{c}{12}\right)\right| = \left|\left(0,0,\frac{c}{4}\right)\right| = \frac{\sqrt{6}}{4}a \tag{32}$$

In the perfect model of the HD and CD phases, all nodes are tetravalent, and the numbers of nodes and struts follow the relation

$$N_{strut} = 2N_{node} \tag{33}$$

However, the nodal valence distributions reflect some defects in the simulated configurations (Figure 7a). The node size distributions of both phases show similar trends with a pronounced unimodal shape and a small-size tail arising from structural defects (Figure 7b), indicating that the conformation of interconnected nodes has a minimal effect on the core assembly behavior.

The structure factor of the simulated HD and CD phases is calculated using the position vectors of GY beads to reveal the periodic symmetry of the network nodes. Based on the

https://doi.org/10.1021/acs.jctc.3c00395
J. Chem. Theory Comput. XXXX, XXX, XXX−XXX

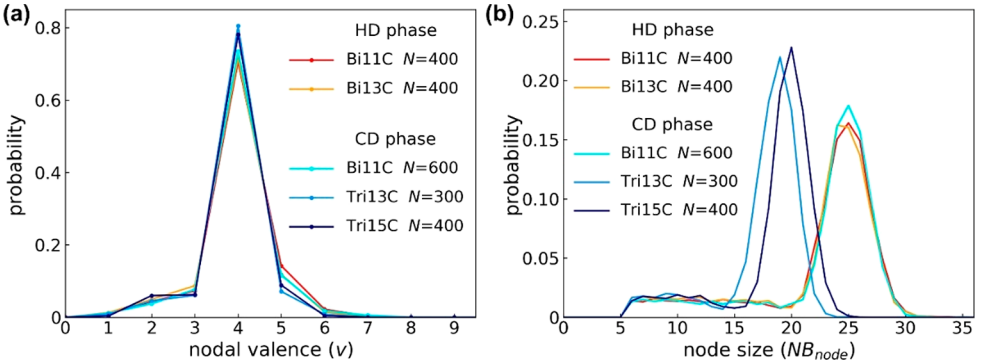

Figure 7. Network-skeleton analysis for the single HD and CD phases formed by representative molecular structures with different system sizes at $T^* = 0.7$.

Table 6. Lattice Parameters of the Single HD and CD Phases Estimated from the Structure Factor

phase	molecule	N	L_{box}/σ	a/σ	b/σ	c/σ	α/deg	β/deg	γ/deg
HD	Bi11C	400	20.02	10.01	14.16	14.16	90	90	90
	Bi13C	400	20.77	10.38	14.69	14.69	90	90	90
CD	Bi11C	600	22.92	12.38	12.38	13.23	90	90	81.8
	Tri11C	400	20.02	10.01	12.66	12.66	90	90	90
	Tri13C	300	18.87	9.44	13.34	13.34	90	90	90
	Tri15C	400	21.47	10.73	13.58	13.58	90	90	90

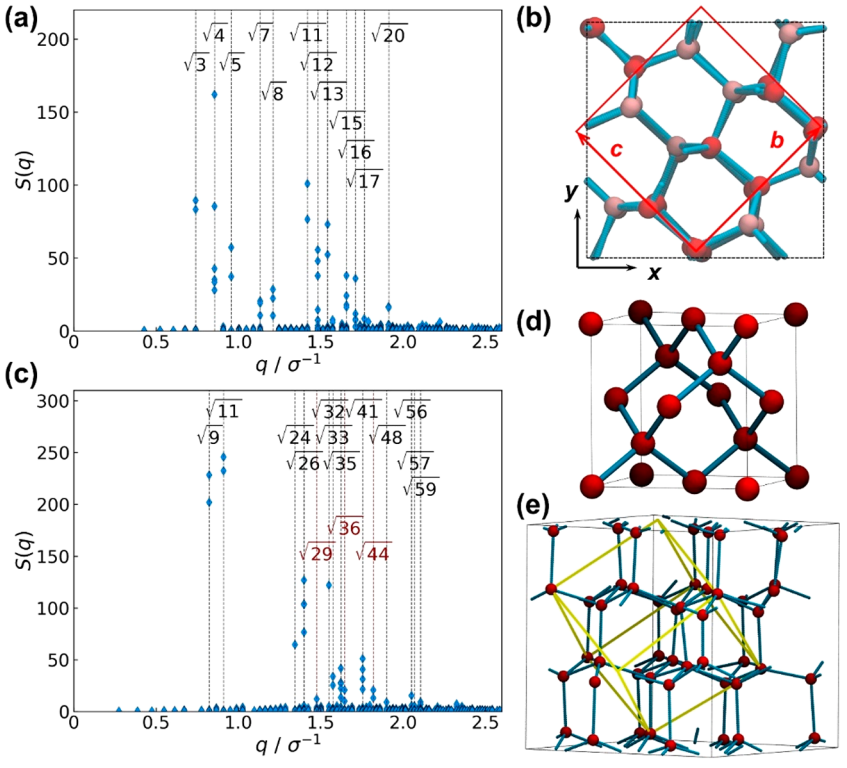

Figure 8. Structure of the single diamond phase formed at $T^* = 0.7$. (a) Structure factor and (b) skeletal graph of HD phase formed by Bi13C with $N = 400$. In (b) struts are blue and nodes are in different shades of red to show their relative positions. (c) Structure factor and (e) skeletal graph of CD phase formed by Bi11C with $N = 600$. For (c), a few extra peaks inconsistent with the theoretical model are marked in red. (d) Theoretical model of the CD network using a representation with a cubic unit cell. In (b) and (e) the unit cell is drawn to illustrate its relationship with the cubic box vectors.

theoretical model of the HD network (eqs 27−29), the related Miller indexed vectors and their magnitude are given by

$$\boldsymbol{G}_{hkl}(\text{HD theory}) = \frac{2\pi}{a}\left(h, \frac{\sqrt{3}}{3}k, \frac{\sqrt{6}}{4}l\right) \tag{34}$$

$$G_{hkl}(\text{HD theory}) = \frac{2\pi}{a}\sqrt{h^2 + \frac{1}{3}k^2 + \frac{3}{8}l^2} \tag{35}$$

Miller indices giving nonzero diffraction intensities are summarized in Table S3 up to a certain magnitude, whose

https://doi.org/10.1021/acs.jctc.3c00395
J. Chem. Theory Comput. XXXX, XXX, XXX−XXX

Table 7. Simulation Conditions and Structural Features for the DD Phases Formed at $T^* = 0.7$[a]

molecule	N	L_{box}/σ	N_{node}	N_{strut}	ν	NB_{node}	NC_{strut}	L_{UC}
Tet13L	400	20.77	48.4	75.7	3.13	16.5	5.21	10.38
Tet15L	400	21.47	50.1	68.9	2.75	16.0	5.74	10.73
Tet17L	330	20.74	46.2	64.7	2.80	14.3	4.94	10.37
Pen13L	350	19.87	43.5	62.5	2.87	16.1	5.44	9.93
Pen15L	350	20.53	46.3	65.9	2.85	15.1	5.14	10.27
Pen19L	320	21.11	47.4	64.4	2.72	13.5	4.79	10.55
Hex13L	300	18.87	40.7	58.4	2.87	14.7	5.00	9.44
Hex15L	300	19.50	40.7	58.0	2.85	14.8	5.00	9.75
Hex19L	300	20.66	45.0	62.0	2.75	13.3	4.56	10.33
Hex21L	270	20.46	42.7	59.4	2.78	12.7	4.21	10.23

[a]The unit cell length (L_{UC}) for the ordered network is estimated from the structure factor.

ratios, calculated with eq 35, are rather complicated due to the noncubic unit cell. For the simulated HD phase, deformed unit cells were determined by the trail-and-error algorithm (Table 6), with the three Miller indexed vectors' basis chosen to be ($\boldsymbol{G}_{110}$, $\boldsymbol{G}_{020}$, $\boldsymbol{G}_{002}$). Taking the Bi13C case (Figure 8a) for illustration, the best-fit relationship is found to be

$$\boldsymbol{G}_{110} = \boldsymbol{q}_{112}, \quad \boldsymbol{G}_{020} = \boldsymbol{q}_{220}, \quad \boldsymbol{G}_{002} = \boldsymbol{q}_{\underline{2}20} \tag{36}$$

$$\begin{cases} \boldsymbol{a}^* = 2\boldsymbol{L}_z^* \\ \boldsymbol{b}^* = \boldsymbol{L}_x^* + \boldsymbol{L}_y^* \\ \boldsymbol{c}^* = -\boldsymbol{L}_x^* + \boldsymbol{L}_y^* \end{cases} \tag{37}$$

The direct lattice vectors in this Bi13C case confirm a deformed unit cell (Figure 8b):

$$\begin{cases} 2\boldsymbol{a} = \boldsymbol{L}_z \\ 2\boldsymbol{b} = \boldsymbol{L}_x + \boldsymbol{L}_y \\ 2\boldsymbol{c} = -\boldsymbol{L}_x + \boldsymbol{L}_y \end{cases} \tag{38}$$

Given the cubic shape of the simulation box, the related Miller indexed vectors and their magnitudes are given by

$$\boldsymbol{G}_{hkl}(\text{HD Bi13C}) = \frac{2\pi}{L_x}(k - l, k + l, 2h) \tag{39}$$

$$G_{hkl}(\text{HD Bi13C}) = \frac{2\pi}{L_x}\sqrt{4h^2 + 2(k^2 + l^2)} \tag{40}$$

Applying the theoretical model, most of the diffraction peaks in the simulated $S(\boldsymbol{q})$ plot are designated by the corresponding Miller indices, but the ratios between them are relatively simple compared with the theoretical ones (Table S3). The presence of these Miller indexed peaks confirms that the periodic symmetry embedded in the theoretical model is well-maintained in the simulated configuration.

For the theoretical model of the CD network, a more conventional representation with a cubic unit cell is used to study the simulated $S(\boldsymbol{q})$ plots rather than using eqs 30−32 for a cuboid unit cell. In this representation, the lattice parameters, the node positions in fractional coordinates, and the strut length are

$$(a, b, c, \alpha, \beta, \gamma) = (a, a, a, 90°, 90°, 90°) \tag{41}$$

$$\text{nodes}\begin{cases} (0,0,0) & \left(\frac{1}{4},\frac{1}{4},\frac{1}{4}\right); \left(\frac{1}{2},\frac{1}{2},0\right) & \left(\frac{3}{4},\frac{3}{4},\frac{1}{4}\right) \\ \left(\frac{1}{2},0,\frac{1}{2}\right) & \left(\frac{3}{4},\frac{1}{4},\frac{3}{4}\right); \left(0,\frac{1}{2},\frac{1}{2}\right) & \left(\frac{1}{4},\frac{3}{4},\frac{3}{4}\right) \end{cases} \tag{42}$$

$$L_{strut} = \left|\left(\frac{1}{4}a, \frac{1}{4}b, \frac{1}{4}c\right)\right| = \frac{1}{4}\sqrt{3}a \tag{43}$$

Miller indices giving nonzero diffraction intensity are summarized in Table S4 up to a certain magnitude. For a general cubic unit cell, the ratios between Miller indices can be calculated using eq 21. For the simulated CD phase, different deformed unit cells were determined by the trail-and-error algorithm (Table 6), in which the basis for the three Miller indexed vectors is chosen to be ($\boldsymbol{G}_{11\underline{1}}$, $\boldsymbol{G}_{1\underline{1}1}$, $\boldsymbol{G}_{1\underline{1}\underline{1}}$). Taking the Bi11C case (Figure 8c) for illustration, the best-fit relationship is found to be

$$\boldsymbol{G}_{11\underline{1}} = \boldsymbol{q}_{300}, \quad \boldsymbol{G}_{1\underline{1}1} = \boldsymbol{q}_{\underline{1}31}, \quad \boldsymbol{G}_{1\underline{1}\underline{1}} = \boldsymbol{q}_{113} \tag{44}$$

$$\begin{cases} 2\boldsymbol{a}^* = 2\boldsymbol{L}_x^* + 3\boldsymbol{L}_y^* + \boldsymbol{L}_z^* \\ 2\boldsymbol{b}^* = 2\boldsymbol{L}_x^* - \boldsymbol{L}_y^* - 3\boldsymbol{L}_z^* \\ \boldsymbol{c}^* = -\boldsymbol{L}_x^* + \boldsymbol{L}_y^* - \boldsymbol{L}_z^* \end{cases} \tag{45}$$

The direct lattice vectors in the Bi11C case confirms a deformed unit cell (Figure 8d,e):

$$\begin{cases} 12\boldsymbol{a} = 4\boldsymbol{L}_x + 5\boldsymbol{L}_y + \boldsymbol{L}_z \\ 12\boldsymbol{b} = 4\boldsymbol{L}_x - \boldsymbol{L}_y - 5\boldsymbol{L}_z \\ 3\boldsymbol{c} = -\boldsymbol{L}_x + \boldsymbol{L}_y - \boldsymbol{L}_z \end{cases} \tag{46}$$

and given the cubic shape of the simulation box, the related Miller indexed vectors and magnitudes are

$$\boldsymbol{G}_{hkl}(\text{CD Bi11C}) = \frac{\pi}{L_x}(2h + 2k - 2l, 3h - k + 2l, h - 3k - 2l) \tag{47}$$

$$G_{hkl}(\text{CD Bi11C}) = \frac{\pi}{L_x}\sqrt{14(h^2 + k^2) + 12l^2 - 4hk} \tag{48}$$

Applying the theoretical model, most of the diffraction peaks in the simulated $S(\boldsymbol{q})$ plot are designated by the corresponding Miller indices (Table S4). A few peaks, which correspond to the completely destructive interference with zero diffraction intensity in the theoretical model, are detected in the $S(\boldsymbol{q})$ plot,

https://doi.org/10.1021/acs.jctc.3c00395
J. Chem. Theory Comput. XXXX, XXX, XXX−XXX

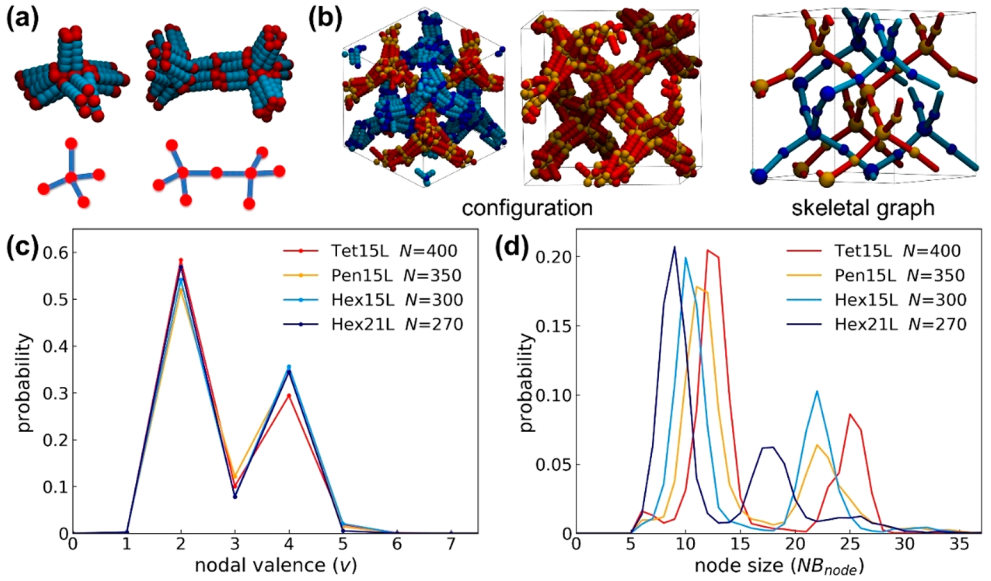

Figure 9. Network characteristics of DD phase formed at $T^* = 0.7$. (a) Basic building unit with struts in blue and nodes in red. (b) Snapshots of phase obtained by Tet15L with $N = 400$. The two interwoven networks are colored differently: One has red struts and yellow nodes, and the other has blue struts and dark blue nodes. Distributions of (c) nodal valence and (d) node size generated by the network-skeleton analysis of representative molecular structures and system sizes.

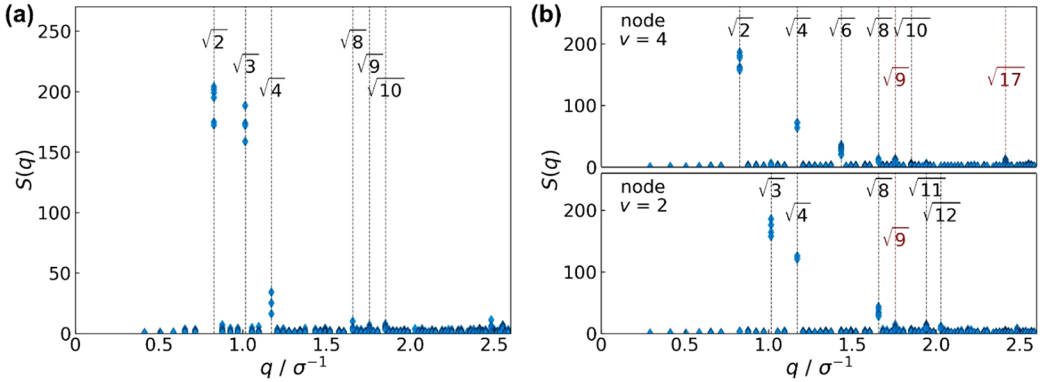

Figure 10. Structure factor analysis for the DD phase from the simulated configuration formed by Tet15L with $N = 400$ at $T^* = 0.7$ using (a) both GY and PH beads and (b) GY beads forming the $v = 4$ nodes (top) and GY beads forming the $v = 2$ nodes (bottom). Extra diffraction peaks inconsistent with the theoretical model are marked in red.

indicating that the periodic symmetry of the CD network is slightly modified by the structural deformation.

In summary, the HD and CD phases were found to be less sensitive to finite size effects, since they can compress and stretch their unit cells along different directions to fit into the simulation box. However, a well-designed and well-sized simulation box may be required to obtain less defective configurations that fully reproduce the theoretical model. We note that the HD and CD phases were occasionally seen as competing phases at the same thermodynamic condition due to their structural similarity, as seen in the simulations of Bi11C with different system sizes.

4.4. Double Diamond Network Phases. The double diamond (DD) network contains two interwoven cubic diamond networks, which are identical but have a translational offset. Assuming that the first network is constructed following the theoretical model of the cubic diamond network from eqs 41−43, the second network can be generated by translating a replica of the first network along any one of the lattice vectors ($\boldsymbol{a}$, $\boldsymbol{b}$, and $\boldsymbol{c}$) by one-half of the unit cell length, $0.5a = 0.5b = 0.5c$. In our simulations, the DD phase was observed at the conditions listed in Table 7. Our network-skeleton analysis shows that this phase can be described by its basic building unit, in which the $v = 4$ nodes are connected by struts containing two bundles of cores in succession (Figure 9a), with the distance between two interconnected nodes being roughly 2 times the core length. Since a node is defined as a cluster of GY beads, an extra "specious" node with $v = 2$ is identified between two interconnected nodes with $v = 4$. This was accounted for by reclassifying struts so that they only contain one bundle of cores. In the perfect model of this DD phase (Figure 9b), all nodes are divided into two groups based on the nodal valence, and each strut is shared by two nodes from each of these two groups. Since each $v = 4$ node is interconnected to four $v = 2$ nodes, and each $v = 2$ node is interconnected to two $v = 4$ nodes, it follows then that

$$N_{\text{node}} = N_{\text{node}}(v = 4) + N_{\text{node}}(v = 2) = 3N_{\text{node}}(v = 4) \quad (49)$$

https://doi.org/10.1021/acs.jctc.3c00395
J. Chem. Theory Comput. XXXX, XXX, XXX−XXX

Table 8. Simulation Conditions and Structural Features for the DG Phases Formed at $T^* = 0.7$

molecule	N	L_{box}/σ	N_{node}	N_{strut}	ν	NB_{node}	NC_{strut}	L_{UC}
Bi17L	400	22.12	42.8	72.9	3.40	18.7	5.28	22.1
Bi21C	300	21.19	34.5	52.7	3.05	17.4	5.56	21.2
Bi25C	330	22.89	39.2	60.4	3.08	16.9	5.28	22.9
Tri13L	300	18.87	30.7	51.5	3.35	19.5	5.52	18.9
Tri17L	300	20.10	33.0	52.6	3.18	18.2	5.39	20.1
Tri21L	280	20.71	33.5	50.8	3.03	16.7	5.27	20.7
Tri17C	250	18.91	29.9	48.9	3.27	16.7	5.00	18.9
Tri21C	250	19.94	31.5	49.6	3.15	15.9	4.90	19.9
Tri25C	250	20.87	33.2	50.2	3.02	15.0	4.88	20.9
Tet17L	250	18.91	30.2	48.2	3.20	16.6	4.94	18.9
Tet17C	200	17.56	26.8	45.5	3.40	15.0	4.31	17.6
Tet21C	180	17.87	26.3	41.3	3.13	13.7	4.24	17.9
Tet25C	170	18.35	26.5	39.9	3.01	12.8	4.10	18.4
Pen19L	200	18.05	27.6	42.5	3.08	14.4	4.47	18.1
Pen19C	150	16.40	22.2	33.9	3.06	13.6	4.26	16.4
Pen23C	150	17.22	24.0	37.4	3.12	12.5	3.85	17.2
Hex21C	100	14.69	16.1	24.0	2.99	12.4	4.09	14.7
Hex23C	100	15.04	16.3	24.3	2.98	12.3	3.93	15.0

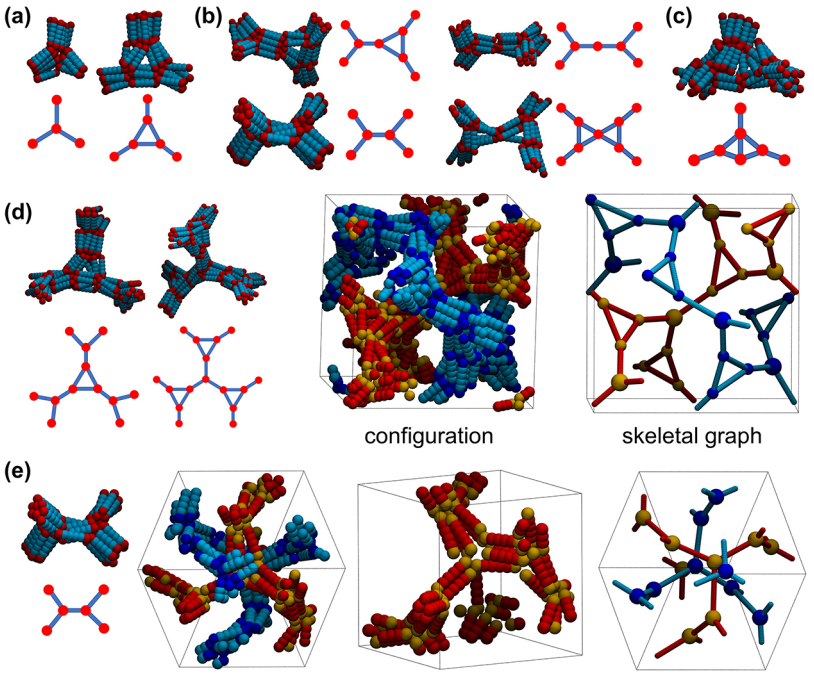

Figure 11. Snapshots of the DG phases formed at $T^* = 0.7$. (a) Basic building units. (b) Interconnecting arrangements between building units. (c) Example of local node structure with less ordered backbone packing. (d) DG1 phase obtained by Tri25C with $N = 250$. (e) DG2 phase obtained by Hex23C with $N = 100$. In most snapshots, struts are blue and nodes are red. In (d) and (e), two interwoven networks are colored differently; one has red struts and yellow nodes, and the other blue struts and dark blue nodes.

$$N_{strut} = 4N_{node}(\nu = 4) = \frac{4}{3}N_{node} \tag{50}$$

In the simulated configurations, the nodal valence distribution confirms two major types of nodes predicted by the perfect model along with some minor defects (Figure 9c). Since the node with larger valence is anticipated to contain more GY beads, the node size distribution displays a bimodal shape with uneven weights (Figure 9d), reflecting the two primary types of nodes and their relative abundances predicted by eq 49.

The structure factor of the simulated DD phases is calculated using the position vectors of both GY beads and PH beads, since nodes and struts together make up the principal periodic features of the DD network. The peak positions in the $S(\boldsymbol{q})$ pattern (Figure 10a) are consistent with the characteristic ratios of ($\sqrt{2}$: $\sqrt{3}$: $\sqrt{4}$: $\sqrt{6}$: $\sqrt{8}$: $\sqrt{9}$).[51] In addition, the nodes alone exhibit different periodic features (Figure 10b). Indeed, the characteristic ratios from the structure factor calculated using the GY beads forming the $\nu = 4$ nodes follow the body-centered-cubic (BCC) symmetry, ($\sqrt{2}$: $\sqrt{4}$: $\sqrt{6}$: $\sqrt{8}$: $\sqrt{10}$), while those using the GY beads forming the specious $\nu = 2$ nodes roughly follow the face-centered-cubic (FCC) symmetry, ($\sqrt{3}$: $\sqrt{4}$: $\sqrt{8}$: $\sqrt{11}$: $\sqrt{12}$). For these three types of cubic periodic symmetry (DD, BCC, and FCC), their unit cell lengths are evaluated using eq 17

https://doi.org/10.1021/acs.jctc.3c00395
J. Chem. Theory Comput. XXXX, XXX, XXX−XXX

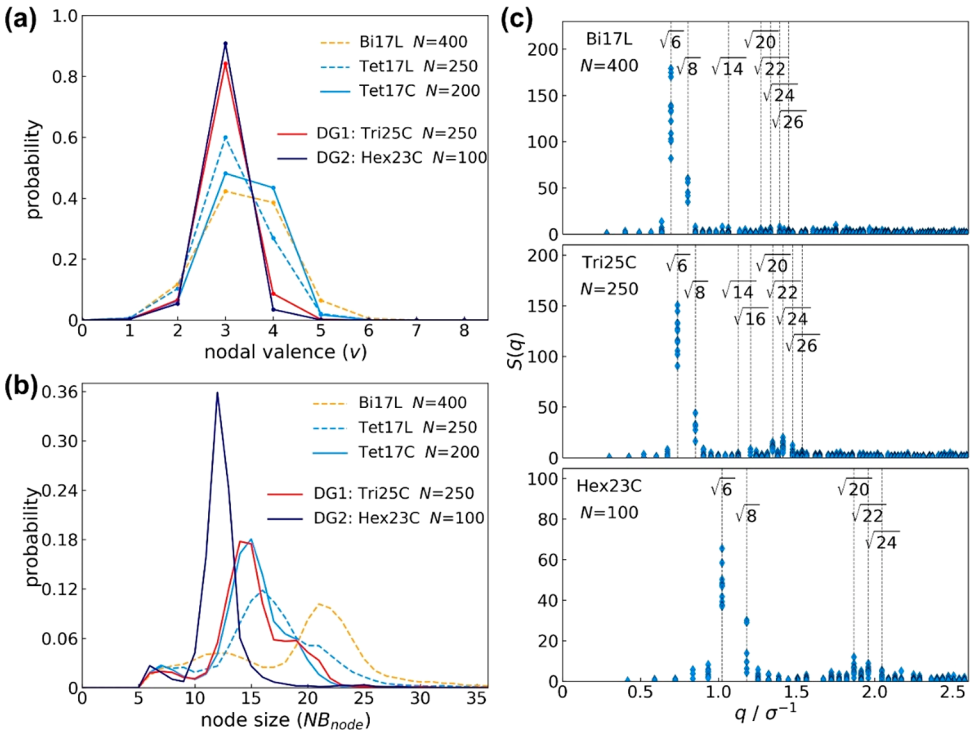

Figure 12. Structure analysis for DG phases formed at $T^* = 0.7$. Distributions of (a) nodal valence and (b) node size generated by the network-skeleton analysis of representative molecular structures with different system sizes. (c) Structure factors from configurations formed by Bi17L, Tri25C, and Hex23C.

with $d = \sqrt{2}$, $\sqrt{2}$, and $\sqrt{3}$, respectively, and all of them are equal to half of the cubic simulation box length, $L_{UC}(DD) = L_{UC}(BCC) = L_{UC}(FCC) = L_{box}/2$. The theoretical models are used to assign proper Miller indices to the diffraction peaks observed in these three $S(q)$ plots (Table S5). Some small mismatches observed in the $S(q)$ plots could be related to variations in the actual volume occupied by the simulated networks (contrasting the dimensionless points in the theoretical model) and some minor structural defects. Note that the BCC symmetry shows the same series of ratios as the simple cubic symmetry in section 4.2 (1: $\sqrt{2}$: $\sqrt{3}$: $\sqrt{4}$: $\sqrt{5}$), but they can be distinguished based on a more detailed analysis of the Miller indices and other metrics.

For the DD phases formed by different molecular structures, our simulation boxes appear to usually accommodate eight unit cells, leading to different cell lengths (Table 7). Furthermore, for the perfect model of the simulated DD phase, one unit cell contains two $\nu = 4$ nodes and four $\nu = 2$ nodes, and the total number of nodes and struts in the eight-unit-cell configuration should be around $N_{node} = 48$ and $N_{strut} = 64$. Results in Table 7 show varying deviations from the perfect model, a likely indicator of the extent of structural defects.

4.5. Double Gyroid Network Phases. The double gyroid (DG) network contains two interwoven gyroid networks with opposite chiralities, and each network consists of three-way-junction nodes with triagonal planar geometry, which are interconnected by a set of struts. In our simulation, the DG network was observed over a wide range of simulation conditions and for different lateral chain shapes and attaching points; some representative conditions are listed in Table 8. These simulated configurations exhibit many variations, as revealed by our network-skeleton analysis, which points to two types of basic building units (Figure 11a): a regular $\nu = 3$ node and a triangle nodal complex whose edges are formed by three bundles of cores and its vertices are formed by three $\nu = 3$ nodes. In addition, the composition of these two building units fluctuates among configurations, and different interconnecting arrangements between building units are identified (Figure 11b), some of which even lead to the formation of $\nu = 4$ nodes. Due to the flexibility and variability of these building units, the packing of cores in the DG network is often less ordered, giving rise to broad distributions of nodal valences and sizes (Figure 12a,b). The unexpected values of nodal valence ($\nu > 3$) are related to the complex interconnecting arrangements mentioned above, to structural defects, and to more complicated moieties only identified in some DG networks with less ordered core packing (Figure 11c).

Among all simulated configurations, two DG phases with well-ordered core packing are selected for illustration. The DG1 phase formed by Tri25C (Figure 11d) consists of both nodal building units with a one-to-one ratio: Each triangle complex is interconnected to three regular $\nu = 3$ nodes by struts containing one bundle of cores, and each regular $\nu = 3$ node is interconnected to three triangle complexes by struts also containing one bundle of cores. In the perfect model of DG1, all nodes have a valence of 3, and the numbers of nodes and struts follow the relation

$$N_{strut} = \frac{3}{2} N_{node} \tag{51}$$

Accordingly, the nodal valence distribution is concentrated around $\nu = 3$, and the node size distribution roughly exhibits a bimodal shape with unequal weights (Figure 12a,b), reflecting the populations of the larger-sized regular nodes and the smaller-sized nodes corresponding to the vertices of the triangle complexes. The DG2 phase formed by Hex23C

https://doi.org/10.1021/acs.jctc.3c00395
J. Chem. Theory Comput. XXXX, XXX, XXX−XXX

(Figure 11e) only contains the regular $v = 3$ nodes, which are interconnected by struts containing one bundle of cores, with the number of nodes and struts in the perfect model also following eq 51. The distributions of nodal valences and sizes for DG2 display a concentrated unimodal shape (Figure 12a,b), indicating a homogeneous core packing within the networks.

The structure factor of the simulated DG phases is calculated using the position vectors of both GY and PH beads, since nodes and struts together make up the principal periodic features of the DG network. In the theoretical model, the DG network can be represented by a cubic unit cell with 16 nodes (eight nodes per single network). The lattice parameters and the node positions in fractional coordinates are listed below, and the complete network is constructed by connecting any two nodes from the same network at a strut-length (L_{strut}) distance:

$$(a, b, c, \alpha, \beta, \gamma) = (a, a, a, 90^\circ, 90^\circ, 90^\circ) \tag{52}$$

$$\text{nodes}\begin{cases}\text{network 1}\begin{cases}(0,0,0) & \left(\frac{1}{4},\frac{1}{4},0\right) & \left(0,\frac{3}{4},\frac{1}{4}\right) & \left(\frac{1}{4},\frac{1}{2},\frac{1}{4}\right)\\ \left(\frac{3}{4},\frac{3}{4},\frac{1}{2}\right) & \left(\frac{1}{2},\frac{1}{2},\frac{1}{2}\right) & \left(\frac{3}{4},0,\frac{3}{4}\right) & \left(\frac{1}{2},\frac{1}{4},\frac{3}{4}\right)\end{cases}\\ \text{network 2}\begin{cases}\left(\frac{1}{2},\frac{3}{4},0\right) & \left(\frac{3}{4},\frac{1}{2},0\right) & \left(\frac{1}{2},0,\frac{1}{4}\right) & \left(\frac{3}{4},\frac{1}{4},\frac{1}{4}\right)\\ \left(\frac{1}{4},0,\frac{1}{2}\right) & \left(0,\frac{1}{4},\frac{1}{2}\right) & \left(\frac{1}{4},\frac{3}{4},\frac{3}{4}\right) & \left(0,\frac{1}{2},\frac{3}{4}\right)\end{cases}\end{cases} \tag{53}$$

$$L_{strut} = \left|\left(\frac{1}{4}a, \frac{1}{4}b, 0\right)\right| = \left|\left(\frac{1}{4}a, 0, \frac{1}{4}c\right)\right| = \left|\left(0, \frac{1}{4}b, \frac{1}{4}c\right)\right| = \frac{1}{4}\sqrt{2}\,a \tag{54}$$

Miller indices giving nonzero diffraction intensity are summarized in Table S6, and ratios between them can be calculated using eq 21. The peak positions in the simulation $S(q)$ plots (Figure 12c) are in good agreement with the characteristic ratios of ($\sqrt{6}$: $\sqrt{8}$: $\sqrt{14}$: $\sqrt{16}$: $\sqrt{20}$: $\sqrt{22}$),[51] with some small shifts. Theoretical models were used to assign proper Miller indices to diffraction peaks observed in these $S(q)$ plots (Table S6). The cubic unit cell length of different simulated configurations evaluated using eq 17 with $d = \sqrt{6}$ indicate that only a single unit cell was present in the simulation boxes employed, leading to a wide range of cell lengths (Table 8).

4.6. Discussion of Molecular and Phase Structures. Given the wide range of molecular structures and self-assembled morphologies explored in our simulations, in this section, we try to identify general trends in the roles of specific molecular features in phase behavior, which may form the basis for rational molecular design strategies.

4.6.1. Lateral Chain Shape. In our model, the incompatibility between the rigid cores and the lateral chains drives them to form separate domains whose interface is influenced by the lateral chain shape. The more branched the lateral chain, the stronger the crowding of AK beads around the rigid cores, which generates a stronger curvature of the interface formed by the core domains. Overall, when the number of branches is increased (going top down in the phase diagram of Figure 3), the assembled structure is observed to change from the lamellar and honeycomb columnar phases with relatively flat interfaces to the network and axial-bundled columnar phases with highly curved interfaces. This effect can be quantified by analyzing special metrics for the packing of lateral beads around a molecular core, as shown in Figure S6a. In addition, the network strut formed by molecules with more branches contains fewer cores due to the stronger crowding around them. As a result, when forming the same ordered network phase with different molecules (as illustrated by SP and DD in Figures 4d, 9d, and S6b), both the strut thickness and the node diameter decrease as the lateral chain shape changes from "Tri" to "Hex", because the node size is mainly determined by the strut thickness for a given nodal valence.

For molecules having the same lateral chain shape (N_{branch}) but different branch lengths (N_{flx}), longer branches generate a stronger crowding of AK beads around the core and a decrease of the strut and node sizes when forming the same ordered network phase. A quantification of this effect is shown in Figure S7a. By extending the branch length in the lateral chain, not only is the distance between neighboring bundles of molecular cores increased, but their relative orientations can also be altered depending on the molecular cross-sectional shape,[6,53] which leads to the formation of different nodal structures. However, these interrelations are nontrivial, and we can only provide some heuristics based on the simulation results. For a wide range of N_{flx} values, increasing the branch length often leads to a decrease of nodal valence in the resulting network phases. A typical example is the trident chain with the center attachment, where a transition is observed from SP ($v = 6$) to CD ($v = 4$) to DG ($v = 3$) along N_{flx} in the phase diagram (Figure 3). Even for the disordered network phases, the average nodal valence is observed to decrease as N_{flx} increases (Figure S7c).

The lateral chain AK bead distributions depicted in Figures S6 and S7 show that the AK beads in a given molecule flare out about the core axis forming a conical density "cloud" that reflects how such chains fill the space around the network's skeleton, with larger flaring correlating with higher interfacial curvature. Similar analyses of side chain shape distributions are relevant to other systems where chains are connected to interfaces and frameworks. For instance, the features of such distributions for single-stranded DNA overhangs protruding out of the arms of a DNA origami hinge[54] can reveal correlations with the shape and stability of the hinge.

4.6.2. Lateral Chain Attachment. The strong self-attraction between GY beads in our model is the major driving force for molecular self-assembly, and these beads can be either bead1 or bead6 based on the relative position to the lateral chain (Figure 1). For the same lateral chain shape, the two types of the attaching arrangements (left and center) can generate different forms of steric hindrance for the clustering of GY beads to alter their assembly behavior. In the left attachment, the lateral chain is much closer to bead1 than to bead6, leading to a higher density of nearby AK beads and thus relatively strong crowding around bead1, while in the center attachment the lateral chain is roughly attached at the middle of the core and the resulting AK bead populations and crowding around bead1 and bead6 are comparable. These qualitative effects can be quantified by analyzing variations in the local density of AK beads as shown in Figure S8a.

Since GY beads tend to cluster into nodes in the network structure, the crowding around them plays an important role in nodal formation. The ordered network phases are associated with preferential types and sizes of nodal structures, while the

https://doi.org/10.1021/acs.jctc.3c00395
J. Chem. Theory Comput. XXXX, XXX, XXX−XXX

disordered networks are often able to accommodate a broader and diverse collection of nodal structures and sizes. We hence examine first disordered networks next, as they are more suitable to capture the average trends in assembly behavior and their relation to the lateral chain attachment. For the same lateral chain shape, the nodal partitioning of bead1 and bead6 (Figure S8b) shows that, for the left attachment, the more crowded bead1 is prone to reside in small nodes, while the less crowded bead6 forms larger nodes because it can associate with more similar beads; these tendencies result in the relatively broad and flat nodal size distributions shown in Figure S8c. For the center attachment, bead1 and bead6 form similarly sized nodes due to their comparable crowding environments, often leading to a narrower, unimodal distribution (Figure S8c).

The node-formation behavior in disordered networks noted above provides the basis for understanding the effect of lateral chain attachment point on the formation of ordered network phases. In our simulations, the SP, HD, and CD network phases are only formed by molecules with the center attachment. Based on our analysis, nodes in these networks exhibit very similar structures with roughly uniform size (Figures 4d and 7b), which is more compatible with the center attachment as reflected by the node-formation behavior of bead1 and bead6 in Figure 13. In contrast, the DD network

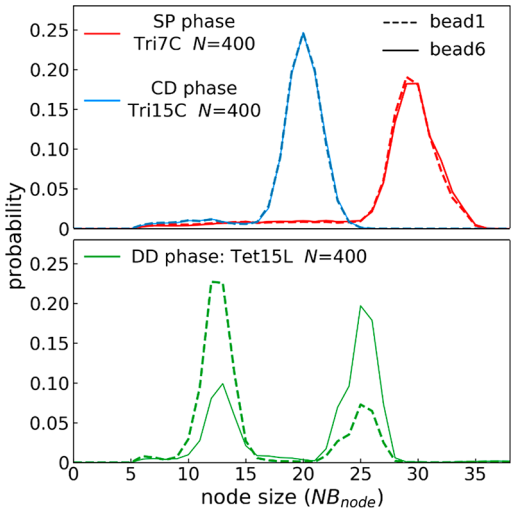

Figure 13. Probability distributions for bead1 and bead6 (terminal beads of the molecular core) residing in nodes of different sizes of selected ordered network phases: SP, CD, and DD. Curves for bead1 and bead6 are marked by dashed and full lines, respectively, and different molecular systems given different colors.

phase is only formed by molecules with the left attachment in which the symmetry between the crowding around the core ends is "broken". Indeed, the bimodal distribution of the node size in the DD network (Figure 9d) turns out to be more compatible with the left attachment, since most of the bead1 sites prefer to form the small $\nu = 2$ nodes and most of the bead6 sites tend to form the big $\nu = 4$ nodes (Figure 13). As for the DG network phases, they are formed by molecules with both left and center attachments largely due to the multiple building units and structural flexibility allowed by this structure, thus limiting the role of any specific node-formation behavior.

4.6.3. Molecular Topology–Morphology Relations. Figure 14 summarizes some of the key correlations observed between molecular topology and network morphologies having distinct nodal valences. These correlations are largely related to how the lateral chain design affects their extent of crowding around the molecular core. For a fixed total length of the lateral chain, the chain shape with more branches can generate a stronger crowding around the molecular core, driving cores to form bundlelike domains with curvier interfaces and thus thinner struts with smaller bundle sizes in the network. For the same lateral chain shape, different branch lengths can fill the space between adjacent molecular-core domains in ways that alter their relative orientations, with longer branches often leading to a decrease of the nodal valence and hence the formation of different network phases. For identical lateral chains, the center attachment, which is nearly center-symmetric about the molecular core, favors network phases with the uniform nodal structure, while the asymmetric left attachment can generate different degrees of crowding at two core ends, facilitating the formation of networks compatible with bidisperse nodal structures.

5. CONCLUSIONS AND OUTLOOK

In this work we studied the phase behavior of bolapolyphiles using molecular dynamics simulations with a simple coarse-grained model developed in our previous computation work.[33,34] At a constant packing fraction of $\eta = 0.45$, different phases are observed depending on the shape, length, and attaching point of the lateral chain, the temperature, and the simulation box length. Among the phases unveiled, our focus centered on several ordered network phases related to the primitive, diamond, and gyroid network phases due to their nontrivial and potentially useful 3D periodic structures. The packing characteristics of these network phases were elucidated by our network-skeleton analysis, and their corresponding periodic symmetries were verified and fully characterized by a detailed structure factor analysis.

Our results allowed us to outline specific trends for the formation of network phases with different nodal valences when the lateral chain length is increased for fixed branching shape and when the number of branches is increased for a fixed number of beads in the lateral chain. Variations in the crowding effect of the lateral chains around the molecular core were examined in some representative molecular structures forming the ordered networks to unveil molecular topology–phase morphology correlations that can serve as the basis for molecular design strategies. In particular, breaking the symmetry between the environments around the two ends of the molecular core by a less symmetric lateral chain attachment point can lead to more complex network phases with bimodal nodal sizes.

Our results illustrate how a simple chemistry-agnostic coarse-grained model can be an effective and useful modeling platform. Our simulated network phases (e.g., SP, CD, DD, and DG) were able to capture the key structural arrangement observed in the experiment, where rodlike mesogen cores are bundled together along their long axes to form the network.[6,28−30] Differences between simulated and experimental phases are mainly related to packing details, such as the average number of rods per bundle. Despite their limitations, our CG model results can provide guidance to future investigations given that most of the specific bolapolyphile designs explored here (for $N_{branch} > 2$) are yet to be studied

https://doi.org/10.1021/acs.jctc.3c00395
J. Chem. Theory Comput. XXXX, XXX, XXX−XXX

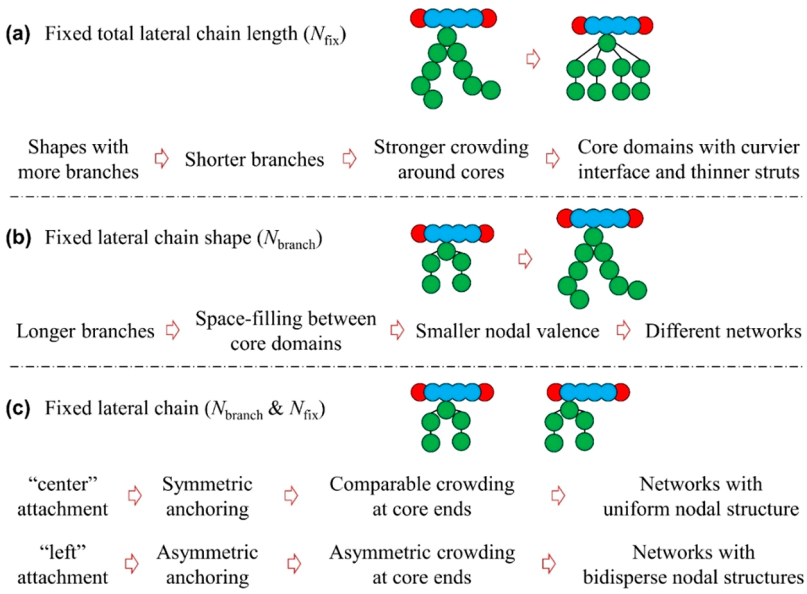

Figure 14. Overview of main molecular topology−morphology trends observed in the multident bolapolyphiles studied.

experimentally. Nevertheless, complementary work is needed to develop chemistry-specific coarse-grained models which can be directly mapped into fully atomistic models to thus describe and predict specific material properties which can be instrumental to determining their suitability for potential applications.[55]

Our findings add to the body of work demonstrating that bolapolyphiles provide a versatile platform to realize a rich variety of ever more complex microstructures. Compared to diblock copolymers, the small size of bolapolyphiles imparts to them the advantage of a much faster self-assembly kinetics and defect annealing. Compared to other more flexible, linear oligomeric amphiphiles, the tendency for the alignment and bundling of the bolapolyphile rigid cores allows them to form intricate structures where such cores form rigid pillars, walls, or skeletons which in some cases resemble those realized by metal−organic frameworks. Indeed, there exist numerous types of honeycomb and network phases which have yet to be realized in other materials' platforms.[1−14,28−32]

While the main goal of this work was to unveil key molecular design features and conditions that are conducive to the formation of different ordered mesophases, going forward, more advanced free-energy-based methods should be used to more quantitatively pinpoint phase transition boundaries. Indeed, while long annealing protocols and repeated runs for different system sizes were performed to ensure the reproducibility of our results, this does not preclude the possibility that some of the phases obtained may have been metastable at the simulated conditions. Furthermore, advanced path sampling techniques could be used to unveil the free-energy barriers and kinetic mechanisms of the disorder-to-order phase transitions which are highly nontrivial for the network phases of interest.[56−58]

■ ASSOCIATED CONTENT

Supporting Information

The Supporting Information is available free of charge at https://pubs.acs.org/doi/10.1021/acs.jctc.3c00395.

Examples of bolapolyphilic molecules; discussion on additional phases; Miller indexed diffraction peaks for the different cubic network phases; lateral chain shape analysis (PDF)

■ AUTHOR INFORMATION

Corresponding Author

Fernando A. Escobedo − *R. F. Smith School of Chemical and Biomolecular Engineering, Cornell University, Ithaca, New York 14853, United States;* orcid.org/0000-0002-4722-9836; Email: fe13@cornell.edu

Author

Yangyang Sun − *R. F. Smith School of Chemical and Biomolecular Engineering, Cornell University, Ithaca, New York 14853, United States;* orcid.org/0000-0002-8499-5425

Complete contact information is available at: https://pubs.acs.org/10.1021/acs.jctc.3c00395

Notes

The authors declare no competing financial interest.

■ ACKNOWLEDGMENTS

Funding support from NSF DMREF Award No. 1922259 and NSF Award CHE-2101829 is gratefully acknowledged. This work used the Extreme Science and Engineering Discovery Environment (XSEDE), which is supported by the National Science Foundation Grant No. ACI-1053575.

■ REFERENCES

(1) Tschierske, C.; Nürnberger, C.; Ebert, H.; Glettner, B.; Prehm, M.; Liu, F.; Zeng, X.-B.; Ungar, G. Complex tiling patterns in liquid crystals. *Interface Focus* **2012**, *2*, 669−680.

(2) Tschierske, C. Development of Structural Complexity by Liquid-Crystal Self-assembly. *Angew. Chem., Int. Ed.* **2013**, *52*, 8828−8878.

(3) Hentrich, F.; Tschierske, C.; Diele, S.; Sauer, C. Molecular design of amphotropic materials: double-headed diol-based mesogens incorporating rigid structural units. *J. Mater. Chem.* **1994**, *4*, 1547−1558.

(4) Cheng, X.; Prehm, M.; Das, M. K.; Kain, J.; Baumeister, U.; Diele, S.; Leine, D.; Blume, A.; Tschierske, C. Calamitic Bolaamphiphiles with (Semi)Perfluorinated Lateral Chains: Polyphilic

Block Molecules with New Liquid Crystalline Phase Structures. *J. Am. Chem. Soc.* **2003**, *125*, 10977−10996.
(5) Prehm, M.; Liu, F.; Zeng, X.; Ungar, G.; Tschierske, C. Axial-Bundle Phases - New Modes of 2D, 3D, and Helical Columnar Self-Assembly in Liquid Crystalline Phases of Bolaamphiphiles with Swallow Tail Lateral Chains. *J. Am. Chem. Soc.* **2011**, *133*, 4906−4916.
(6) Zeng, X.; Prehm, M.; Ungar, G.; Tschierske, C.; Liu, F. Formation of a Double Diamond Cubic Phase by Thermotropic Liquid Crystalline Self-Assembly of Bundled Bolaamphiphiles. *Angew. Chem., Int. Ed.* **2016**, *55*, 8324−8327.
(7) Cheng, X.; Das, M. K.; Baumeister, U.; Diele, S.; Tschierske, C. Liquid Crystalline Bolaamphiphiles with Semiperfluorinated Lateral Chains: Competition between Layerlike and Honeycomb-Like Organization. *J. Am. Chem. Soc.* **2004**, *126*, 12930−12940.
(8) Cheng, X.; Dong, X.; Huang, R.; Zeng, X.; Ungar, G.; Prehm, M.; Tschierske, C. Polygonal Cylinder Phases of 3-Alkyl-2,5-diphenylthiophene-Based Bolaamphiphiles: Changing Symmetry by Retaining Net Topology. *Chem. Mater.* **2008**, *20*, 4729−4738.
(9) Cheng, X.; Dong, X.; Wei, G.; Prehm, M.; Tschierske, C. Liquid-Crystalline Triangle Honeycomb Formed by a Dithiophene-Based X-Shaped Bolaamphiphile. *Angew. Chem., Int. Ed.* **2009**, *48*, 8014−8017.
(10) Chen, C.; Poppe, M.; Poppe, S.; Tschierske, C.; Liu, F. Liquid Organic Frameworks: A Liquid Crystalline 8-Connected Network with Body-Centered Cubic Symmetry. *Angew. Chem., Int. Ed.* **2020**, *59*, 20820−20825.
(11) Liu, F.; Prehm, M.; Zeng, X.; Ungar, G.; Tschierske, C. Two- and Three-Dimensional Liquid-Crystal Phases from Axial Bundles of Rodlike Polyphiles: Segmented Cylinders, Crossed Columns, and Ribbons between Sheets. *Angew. Chem., Int. Ed.* **2011**, *50*, 10599−10602.
(12) Kieffer, R.; Prehm, M.; Pelz, K.; Baumeister, U.; Liu, F.; Hahn, H.; Lang, H.; Ungar, G.; Tschierske, C. Siloxanes and carbosilanes as new building blocks for T-shaped bolaamphiphilic LC molecules. *Soft Matter* **2009**, *5*, 1214−1227.
(13) Kieffer, R.; Prehm, M.; Glettner, B.; Pelz, K.; Baumeister, U.; Liu, F.; Zeng, X.; Ungar, G.; Tschierske, C. X-Shaped polyphilics: liquid crystal honeycombs with single-molecule walls. *Chem. Commun.* **2008**, 3861−3863.
(14) Poppe, S.; Chen, C.; Liu, F.; Tschierske, C. A skeletal double gyroid formed by single coaxial bundles of catechol based bolapolyphiles. *Chem. Commun.* **2018**, *54*, 11196−11199.
(15) Finnefrock, A. C.; Ulrich, R.; Toombes, G. E. S.; Gruner, S. M.; Wiesner, U. The Plumber's Nightmare:[1] A New Morphology in Block Copolymer-Ceramic Nanocomposites and Mesoporous Aluminosilicates. *J. Am. Chem. Soc.* **2003**, *125*, 13084−13093.
(16) Uehara, H.; Yoshida, T.; Kakiage, M.; Yamanobe, T.; Komoto, T.; Nomura, K.; Nakajima, K.; Matsuda, M. Nanoporous Polyethylene Film Prepared from Bicontinuous Crystalline/Amorphous Structure of Block Copolymer Precursor. *Macromolecules* **2006**, *39*, 3971−3974.
(17) Zhou, M.; Nemade, P. R.; Lu, X.; Zeng, X.; Hatakeyama, E. S.; Noble, R. D.; Gin, D. L. New Type of Membrane Material for Water Desalination Based on a Cross-Linked Bicontinuous Cubic Lyotropic Liquid Crystal Assembly. *J. Am. Chem. Soc.* **2007**, *129*, 9574−9575.
(18) Kerr, R. L.; Miller, S. A.; Shoemaker, R. K.; Elliott, B. J.; Gin, D. L. New Type of Li Ion Conductor with 3D Interconnected Nanopores via Polymerization of a Liquid Organic Electrolyte-Filled Lyotropic Liquid-Crystal Assembly. *J. Am. Chem. Soc.* **2009**, *131*, 15972−15973.
(19) Crossland, E. J. W.; Kamperman, M.; Nedelcu, M.; Ducati, C.; Wiesner, U.; Smilgies, D.-M.; Toombes, G. E. S.; Hillmyer, M. A.; Ludwigs, S.; Steiner, U.; Snaith, H. J. A Bicontinuous Double Gyroid Hybrid Solar Cell. *Nano Lett.* **2009**, *9*, 2807−2812.
(20) Crossland, E. J. W.; Nedelcu, M.; Ducati, C.; Ludwigs, S.; Hillmyer, M. A.; Steiner, U.; Snaith, H. J. Block Copolymer Morphologies in Dye-Sensitized Solar Cells: Probing the Photovoltaic Structure-Function Relation. *Nano Lett.* **2009**, *9*, 2813−2819.
(21) Orilall, M. C.; Wiesner, U. Block copolymer based composition and morphology control in nanostructured hybrid materials for energy conversion and storage: solar cells, batteries, and fuel cells. *Chem. Soc. Rev.* **2011**, *40*, 520−535.
(22) Maldovan, M.; Urbas, A. M.; Yufa, N.; Carter, W. C.; Thomas, E. L. Photonic properties of bicontinuous cubic microphases. *Phys. Rev. B* **2002**, *65*, 165123.
(23) Stefik, M.; Guldin, S.; Vignolini, S.; Wiesner, U.; Steiner, U. Block copolymer self-assembly for nanophotonics. *Chem. Soc. Rev.* **2015**, *44*, 5076−5091.
(24) Dolan, J. A.; Wilts, B. D.; Vignolini, S.; Baumberg, J. J.; Steiner, U.; Wilkinson, T. D. Optical Properties of Gyroid Structured Materials: From Photonic Crystals to Metamaterials. *Adv. Opt. Mater.* **2015**, *3*, 12−32.
(25) Saranathan, V.; Osuji, C. O.; Mochrie, S. G. J.; Noh, H.; Narayanan, S.; Sandy, A.; Dufresne, E. R.; Prum, R. O. Structure, function, and self-assembly of single network gyroid ($I4_132$) photonic crystals in butterfly wing scales. *Proc. Natl. Acad. Sci. U.S.A.* **2010**, *107*, 11676−11681.
(26) Wilts, B. D.; Michielsen, K.; De Raedt, H.; Stavenga, D. G. Hemispherical Brillouin zone imaging of a diamond-type biological photonic crystal. *J. R. Soc. Interface* **2012**, *9*, 1609−1614.
(27) Han, L.; Che, S. An Overview of Materials with Triply Periodic Minimal Surfaces and Related Geometry: From Biological Structures to Self-Assembled Systems. *Adv. Mater.* **2018**, *30*, 1705708.
(28) Poppe, S.; Cheng, X.; Chen, C.; Zeng, X.; Zhang, R.-B.; Liu, F.; Ungar, G.; Tschierske, C. Liquid Organic Frameworks: The Single-Network "Plumber's Nightmare" Bicontinuous Cubic Liquid Crystal. *J. Am. Chem. Soc.* **2020**, *142*, 3296−3300.
(29) Zeng, X.; Poppe, S.; Lehmann, A.; Prehm, M.; Chen, C.; Liu, F.; Lu, H.; Ungar, G.; Tschierske, C. A Self-Assembled Bicontinuous Cubic Phase with a Single-Diamond Network. *Angew. Chem., Int. Ed.* **2019**, *58*, 7375−7379.
(30) Liu, F.; Prehm, M.; Zeng, X.; Tschierske, C.; Ungar, G. Skeletal Cubic, Lamellar, and Ribbon Phases of Bundled Thermotropic Bolapolyphiles. *J. Am. Chem. Soc.* **2014**, *136*, 6846−6849.
(31) Poppe, M.; Chen, C.; Ebert, H.; Poppe, S.; Prehm, M.; Kerzig, C.; Liu, F.; Tschierske, C. Transition from nematic to gyroid-type cubic soft self-assembly by side-chain engineering of π-conjugated sticky rods. *Soft Matter* **2017**, *13*, 4381−4392.
(32) Chen, C.; Kieffer, R.; Ebert, H.; Prehm, M.; Zhang, R.-B.; Zeng, X.; Liu, F.; Ungar, G.; Tschierske, C. Chirality Induction through Nano-Phase Separation: Alternating Network Gyroid Phase by Thermotropic Self-Assembly of X-Shaped Bolapolyphiles. *Angew. Chem., Int. Ed.* **2020**, *59*, 2725−2729.
(33) Crane, A. J.; Martínez-Veracoechea, F. J.; Escobedo, F. A.; Müller, E. A. Molecular dynamics simulation of the mesophase behaviour of a model bolaamphiphilic liquid crystal with a lateral flexible chain. *Soft Matter* **2008**, *4*, 1820−1829.
(34) Sun, Y.; Padmanabhan, P.; Misra, M.; Escobedo, F. A. Molecular dynamics simulation of thermotropic bolaamphiphiles with a swallow-tail lateral chain: formation of cubic network phases. *Soft Matter* **2017**, *13*, 8542−8555.
(35) Bates, M.; Walker, M. Dissipative particle dynamics simulation of T- and X-shaped polyphilic molecules exhibiting honeycomb columnar phases. *Soft Matter* **2009**, *5*, 346−353.
(36) Bates, M. A.; Walker, M. Dissipative particle dynamics simulation of quaternary bolaamphiphiles: multi-colour tiling in hexagonal columnar phases. *Phys. Chem. Chem. Phys.* **2009**, *11*, 1893−1900.
(37) Bates, M. A.; Walker, M. Computer Simulation of the Pentagonal Columnar Phase of Liquid Crystalline Bolaamphiphiles. *Mol. Cryst. Liq. Cryst.* **2010**, *525*, 204−211.
(38) Bates, M. A.; Walker, M. Computer simulation of the columnar phases of liquid crystalline bolaamphiphiles. *Liq. Cryst.* **2011**, *38*, 1749−1757.
(39) Liu, X.; Yang, K.; Guo, H. Dissipative Particle Dynamics Simulation of the Phase Behavior of T-Shaped Ternary Amphiphiles

https://doi.org/10.1021/acs.jctc.3c00395
J. Chem. Theory Comput. XXXX, XXX, XXX−XXX

Possessing Rodlike Mesogens. *J. Phys. Chem. B* **2013**, *117*, 9106−9120.
(40) Fayaz-Torshizi, M.; Müller, E. A. Coarse-grained molecular dynamics study of the self-assembly of polyphilic bolaamphiphiles using the SAFT-γ Mie force field. *Mol. Syst. Des. Eng.* **2021**, *6*, 594−608.
(41) Weeks, J. D.; Chandler, D.; Andersen, H. C. Role of Repulsive Forces in Determining the Equilibrium Structure of Simple Liquids. *J. Chem. Phys.* **1971**, *54*, 5237−5247.
(42) Plimpton, S. Fast Parallel Algorithms for Short-Range Molecular Dynamics. *J. Comput. Phys.* **1995**, *117*, 1−19.
(43) Thompson, A. P.; Aktulga, H. M.; Berger, R.; Bolintineanu, D. S.; Brown, W. M.; Crozier, P. S.; in 't Veld, P. J.; Kohlmeyer, A.; Moore, S. G.; Nguyen, T. D.; Shan, R.; Stevens, M. J.; Tranchida, J.; Trott, C.; Plimpton, S. J. LAMMPS - a flexible simulation tool for particle-based materials modeling at the atomic, meso, and continuum scales. *Comput. Phys. Commun.* **2022**, *271*, 108171.
(44) Humphrey, W.; Dalke, A.; Schulten, K. VMD: Visual molecular dynamics. *J. Mol. Graphics* **1996**, *14*, 33−38.
(45) Ahmed, A.; Sadus, R. J. Phase diagram of the Weeks-Chandler-Andersen potential from very low to high temperatures and pressures. *Phys. Rev. E* **2009**, *80*, 061101.
(46) Schubert, E.; Sander, J.; Ester, M.; Kriegel, H. P.; Xu, X. DBSCAN Revisited, Revisited: Why and How You Should (Still) Use DBSCAN. *ACM Trans. Database Syst.* **2017**, *42*, 1−21.
(47) Schultz, A. J.; Hall, C. K.; Genzer, J. Obtaining Concentration Profiles from Computer Simulation Structure Factors. *Macromolecules* **2007**, *40*, 2629−2632.
(48) Toby, B. H.; Von Dreele, R. B. *GSAS-II*: the genesis of a modern open-source all purpose crystallography software package. *J. Appl. Crystallogr.* **2013**, *46*, 544−549.
(49) Hailey, A. K.; Hiszpanski, A. M.; Smilgies, D.-M.; Loo, Y.-L. *The Diffraction Pattern Calculator (DPC)* toolkit: a user-friendly approach to unit-cell lattice parameter identification of two-dimensional grazing-incidence wide-angle X-ray scattering data. *J. Appl. Crystallogr.* **2014**, *47*, 2090−2099.
(50) Savikhin, V.; Steinrück, H.-G.; Liang, R.-Z.; Collins, B. A.; Oosterhout, S. D.; Beaujuge, P. M.; Toney, M. F. *GIWAXS-SIIRkit*: scattering intensity, indexing and refraction calculation toolkit for grazing-incidence wide-angle X-ray scattering of organic materials. *J. Appl. Crystallogr.* **2020**, *53*, 1108−1129.
(51) Hyde, S. T. Bicontinuous structures in lyotropic liquid crystals and crystalline hyperbolic surfaces. *Curr. Opin. Solid State Mater. Sci.* **1996**, *1*, 653−662.
(52) Martínez-Veracoechea, F. J.; Escobedo, F. A. Lattice Monte Carlo Simulations of the Gyroid Phase in Monodisperse and Bidisperse Block Copolymer Systems. *Macromolecules* **2005**, *38*, 8522−8531.
(53) Zeng, X.; Ungar, G.; Impéror-Clerc, M. A triple-network tricontinuous cubic liquid crystal. *Nat. Mater.* **2005**, *4*, 562−567.
(54) Shi, Z.; Arya, G. Free energy landscape of salt-actuated reconfigurable DNA nanodevices. *Nucleic Acids Res.* **2020**, *48*, 548−560.
(55) Nowak, C.; Misra, M.; Escobedo, F. A. Framework for Inverse Mapping Chemistry-Agnostic Coarse-Grained Simulation Models into Chemistry-Specific Models. *J. Chem. Inf. Model.* **2019**, *59*, 5045−5056.
(56) Mukhtyar, A. J.; Escobedo, F. A. Developing Local Order Parameters for Order-Disorder Transitions From Particles to Block Copolymers: Methodological Framework. *Macromolecules* **2018**, *51*, 9769−9780.
(57) Mukhtyar, A. J.; Escobedo, F. A. Developing Local Order Parameters for Order-Disorder Transitions From Particles to Block Copolymers: Application to Macromolecular Systems. *Macromolecules* **2018**, *51*, 9781−9788.
(58) Mukhtyar, A. J.; Escobedo, F. A. Computing free energy barriers for the nucleation of complex network mesophases. *J. Chem. Phys.* **2022**, *156*, 034502.

https://doi.org/10.1021/acs.jctc.3c00395
J. Chem. Theory Comput. XXXX, XXX, XXX−XXX